UNIVERSITY OF OSLO
Department of
Geosciences
MetOs Section

High-resolution ensemble forecasts of a polar low by non-hydrostatic downscaling

Master Thesis in Geosciences Meteorology and Oceanography

Silje Lund Sørland

September 1, 2009

Abstract

A short range, limited area ensemble prediction system, LAMEPS, is currently in operational use at the Norwegian Meteorological Institute. It employs 3D-Var for 6 hourly data assimilation cycling for analysis of the control forecast. Initial time and lateral boundaries ensemble perturbations are computed from the 20 + 1 member TEPS (targeted EPS at ECMWF). LAMEPS is run with the quasi-hydrostatic model HIRLAM version 7.1.4. on a 12 km horizontal grid mesh. In this study we have downscaled each LAMEPS member with the non-hydrostatic UK Met Office Unified Model (UM) version 6.1 in order to study the predictability and the predictions of extreme weather related to a polar low observed in the Barents and Norwegian Seas between 3 and 4 March 2008. This event was extensively covered by the observation campaign of the IPY-THORPEX project. UM is in this study configured with 4 km horizontal grid mesh. The domain size has been investigated by using two different domains, one with 390×490 and one with 300×300 grid points. Furthermore, the sensitivity to the physical parameterization in the stable boundary layer has also been explored.

Regular observation data, satellite data, and IPY-THORPEX campaign data have been used to compare with the ensemble forecasts. Probabilities of different meteorological parameters and occurrence of extreme weather events have been studied along with ensemble means, ensemble spread and control runs. In addition, two new model diagnostics for comparing against observation data have been developed. These are cloud top temperatures and tracking of the polar lows path. The ensemble forecast shows clear improvements by increasing horizontal resolution with non-hydrostatic dynamics. However, the size of the integration domain affects the prediction substantially. The improvements are greatest for the large domain. The forecasts are also sensitive to the physical parameterization. The experiments with less vertical mixing in the stable boundary layer reduce the area of high probability for the large domain. The results of the tracking algorithm, which finds the strongest mesoscale track in each ensemble member, show that the location of the strongest track depends on domain size and the perturbation of the physics.

Acknowledgements

During this master thesis I have been assisted and inspired by several people. First of all I would thank my adviser Trond Iversen for giving me this interesting and highly relevant thesis. The help I got from my two co-advisers, Jørn Kristiansen and Morten A. Ø. Køltzow, has been indispensable. A special thanks to Jørn for being especially encouraging every day through the whole year. I'm also very happy I got to participate on the IPY-THORPEX conference in Rømskog and the SRNWP-EPS workshop in Exeter. I'm grateful to Øyvind Sætra for providing me with the observation data from the IPY-THORPEX campaign, Marit Helene Jensen for supplying me with the scripts for the standard analysis tools at met.no and Thor Erik Nordeng for valuable discussions. A special thanks to Kevin Hodges for sharing the tracking algorithm which was very interesting and fun to work with, and I'm very thankful for his quick email replies.

I will also acknowledge David Weir, Kelly McCusker and Maria Sand for proof reading my thesis, and supporting me when I had run out of faith. I'm also very thankful to Haldis Berge for being my latex oracle (and for "suffering" through the summer at CIENS). And I'm very grateful to my family and friends for their (fake?) enthusiasm about polar lows and for their always reliable support. In the end, the days at CIENS would not have been the same without my student fellows. The lunches, coffee breaks and other (food related...) activities made this year!

Contents

Chapter 1

Introduction

Polar lows are intense, mesoscale vortices that develop during cold air outbreaks over a warmer ocean, usually poleward of the polar front (Rassmussen and Turner, 2003). These features often produce heavy precipitation and strong winds, and occur frequently along the coast of Norway during winter. Since polar lows are commonly accompanied by severe weather which may cause great risk to human life and property, it is particularly important to forecast these phenomena with a high degree of accuracy. Numerical Weather Prediction (NWP) models are important for polar low forecasting. However, due to sparse observational data, their small scale structure, and their rapid development, it is challenging to predict polar lows. Further, because of the chaotic nature of the atmosphere, small errors in the initial conditions will grow with lead time and in this way gradually deteriorate the quality of a single deterministic forecast (Lorenz, 1963). Model deficiencies are also a source of forecast error, which reduces the skill of the deterministic forecast. In addition, for limited area modeling (LAM), the lateral boundary data also introduce errors in the forecasts (Gustafsson et al., 1998). As a result of these sources of forecast error, deterministic forecasts are generally not sufficient when predicting polar lows and associated extreme weather.

An ensemble prediction system (EPS) should take into account all these sources of forecast errors, and in this way forecast the actual predictability of the atmosphere. An EPS consist of a range of individual forecasts, i.e. ensemble members, where each member uses slightly different initial conditions. The error growth in a forecast is flow-dependent, which means that in a regime of high predictability, the error growth is much smaller than when the weather is very unpredictable. The spread between the different ensemble members gives an indication of the actual predictability of the atmosphere. The different initial conditions are constructed from the analysis which has been perturbed, except the control run which is unperturbed. At the European Centre for Medium-Range Weather Forecasts (ECMWF) the perturbations added to the initial conditions are based upon a mathematical method called singular vector decomposition (Buizza and Palmer, 1995; Molteni et al., 1996). The model deficiencies have been included in the ensemble system by stochastically perturbing the model physics (Buizza et al., 1999). By constraining the perturbation norm to a specific area, the singular vectors will seek the perturbations with largest norm at final time (e.g. 48 h). This method of constructing targeted EPS (TEPS) with target over Northern Europe for 48

h singular vectors has showed improvement in forecast skill (Frogner and Iversen, 2001). At the Norwegian Meteorological Institute (met.no), the TEPS is used to construct initial and lateral perturbations to a High Resolution Limited Area Model, HIRLAM, and in this manner a high resolution Limited Area Modeling Ensemble Prediction System (LAMEPS) is obtained. HIRLAM is a quasi-hydrostatic model and its LAMEPS configuration is a 12 km horizontal grid mesh. LAMEPS has, to a large extent, improved the forecasting of high impact weather, but the resolution is still too coarse to resolve many important mesoscale features (Jensen et al., 2006).

It is thought that with increased horizontal resolution, the predictability of the mesoscales will be enhanced (e.g. Mass et al., 2002). Hence to better investigate the smaller scales over an area of interest, dynamical downscaling is performed. In dynamical downscaling a global or regional coarse resolution model provides initial and lateral boundary conditions (LBCs) to a model with higher resolution. The higher resolution model does not produce its own analysis. It is intended that the high resolution model should produce realistic, fine-scale details over a region, and in particular where surface structures have fine details. However, dynamical downscaling is not straight forward, and several studies indicate that domain size, location, horizontal resolution, and lateral boundary conditions, in addition to the models' representation of topography, vegetation, and physical descriptions, all affect the model results (e.g. Laprise et al., 2000; Xue et al., 2007; Branković et al., 2008). For instance, Xue et al. (2007) found that forecast results were crucially dependent on the domain size, LBCs, and grid spacing, and emphasized the point that a small domain may hamper the improvements in the forecast. If the domain is small enough it will be too controlled by the lateral boundaries. The domain should be large enough to be able to spin-up small scale features not present in the initial or lateral conditions. Xue et al. (2007) also investigated the effect of the location of the domains, and it was observed that information lost at the lateral boundaries was hard to reproduce in the simulations within the new domain.

In this study, the 21 members of 12 km resolution LAMEPS are downscaled by the UK Met Office Unified Model (UM) with 4 km resolution. In this way a very high-resolution ensemble prediction system, UM-EPS, is obtained. The sensitivity of the size of the domain has been investigated by employing two different domains with 300×300 and 390×490 grid points, but both configurations have a horizontal grid spacing of 4 km. The main goal of this study is to see how much new information is added with a very high resolution ensemble prediction system, as well as how the skill in predicting high impact weather is influenced. UM-EPS has therefore been tested on a polar low event that was extensively observed during the IPY-THORPEX campaign (IPY-THORPEX, 2009), one of the projects during the International Polar Year (IPY, 2009). Also, a more realistic dynamical core will be investigated, since HIRLAM is a quasi-hydrostatic model where the convection is parameterized while UM is a non-hydrostatic model, which allows for high vertical velocities and accelerations, and the convection is partly resolved explicitly and partly parameterized (Lean et al., 2008). Ensemble mean and the spread between the members, together with forecast probabilities, have been compared with regular observation data as well as observation data from the campaign. In addition to

these more conventional verification methods, two new methods to evaluate the forecasts have been included: (1) Pseudo satellite images calculated from model prognostic fields and, (2) a tracking methodology to track polar lows. The pseudo-satellite images are adopted from a method originally developed for HIRLAM (Tijm, 2004). The tracking scheme of Hodges (1994, 1995, 1999) has been used with the aim to track the mesoscale cyclones in UM-EPS.

This thesis is divided as follows: The background for this study is given in Chapter 2, where first a review of the predictability of weather will be given. Then the dynamical downscaling performed in this study will be described. Chapter 2 ends with an introduction to polar lows where there will be a closer description of the polar low observed during the IPY-THORPEX campaign. The verification methodology will be presented in Chapter 3, followed by the results in Chapter 4 and a discussion in Chapter 5. We end with some concluding remarks and ideas for future work.

Chapter 2

Background

2.1 Predictability of weather

Numerical weather prediction (NWP) is an initial value problem, where the ability to make skillful forecasts depends on the realism of the atmosphere and the boundary conditions in NWP models, and to know the initial conditions accurately (Kalnay, 2003). These two sources of inaccuracies may contribute to amplifying the forecast errors and deteriorate the quality of a single deterministic forecast with lead time. When the errors are saturated the errors grow no further and the predictability limit is reached. At that stage the forecast will not add any new information compared to climate statistics. The predictability of the atmosphere varies from day to day, because the error growth depends on the actual weather conditions. A complete forecast thus also forecast the predictability of the atmosphere. Ensemble prediction is a method to integrate ensembles of deterministic forecasts in order to estimate the probability density function (PDFs) of forecasted states (Buizza, 2002). In this way an ensemble prediction system (EPS) will forecast for how long time the weather can be predicted. This section gives an introduction to predictability of weather and EPSs, with emphasis on the EPS applied at European Centre for Medium Range Weather Forecasts (ECMWF).

Critical dependence on the initial conditions

In 1904 the Norwegian meteorologist Vilhelm Bjerknes proposed that the atmosphere is a deterministic system, where all states at a given time can be solved with the physical laws if only the initial state is known. But unfortunately the initial state cannot be of infinite accuracy, and will always contain a tiny error. Lorenz (1963) discovered the critical dependence on the initial conditions with his famous coffee break, where he did the same forecast twice just with a small initial round off error in difference, and surprisingly the results gradually developed very differently. If the flow was periodic, the small error from the round off should have returned to the initial state. Due to this non-periodicity and since there was a critical dependence on the initial conditions, Lorenz realized that chaos is prevalent for atmospheric flows (Lorenz, 1963). In his experiments Lorenz used a highly truncated set of convection equations which was represented in a 3D phase space (Lorenz equations):
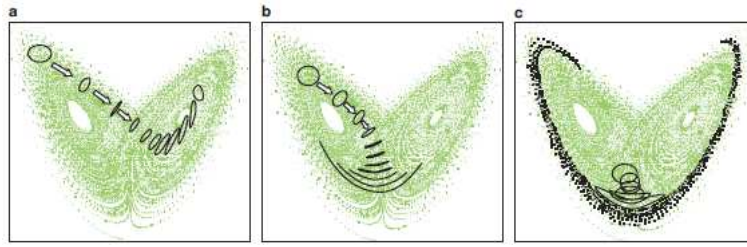
Figure 2.1: *The Lorenz attractor. See text for explanations. Figure adapted from Palmer et al. (2006).*

$$\frac{dx}{dt} = \sigma(y - x) \tag{2.1}$$

$$\frac{dy}{dt} = rx - y - xz \tag{2.2}$$

$$\frac{dz}{dt} = xy - bz \tag{2.3}$$

The parameters σ, r and b are kept constant with the integration, and Lorenz set these parameters to σ=10, r=28 and b=8/3. This resulted in fully non-periodic solutions and chaotic behavior and the set of all possible solutions are called the Lorenz attractor. The two wings of the attractor can be considered as two different flow regimes. Figure 2.1 shows the flow obtained by integrating the equations several times with slightly different initial conditions, and Figure 2.1a, b and c show three different sets of the initial conditions and the evolution with time. In 2.1a the system is in a highly predictable initial state, as all points stay close together with time. A less predictable state is shown in 2.1b, where the points stay close in the beginning, but after a while begin to diverge. In 2.1c there is very short predictability, since all the points diverge early in the forecast and end up far from each other. Figure 2.1 illustrates the basis for ensemble prediction, where the predictability of the atmosphere is dependent on the initial state (Palmer et al., 2006).

Ensemble prediction systems

Lorenz (1963) discovered that the forecast skill is critically dependent on the initial conditions as a consequence of instabilities in the atmosphere. The unstable processes in the atmosphere determine how fast the small initial errors will grow and how far into the future before the predictability limit is reached. Lorenz (1969) estimated the weather predictability limit to about two weeks. However, the error growth is faster at the smaller scales than the larger scales and reach the predictability limit first (Lorenz, 1969). Furthermore, since the predictability is flow dependent, the value of a forecast would be highly enhanced if in addition the predictability is forecasted. This can be done

by adding small perturbations to the analysis. By integrating the different initial states, a range of different forecasts are obtained, and the spread among the forecasts gives an indication of the predictability of the day. ECMWF has routinely employed an ensemble prediction system since 1992, and is using singular vectors for generating the ensemble members (see Buizza and Palmer, 1995; Molteni et al., 1996). The singular vectors are computed with the tangent linear model (TLM) and its adjoint with total energy inner product, thus the perturbation with fastest linear growth over an optimization time of 48 hours are chosen. The singular vectors are targeted to seek the maximum perturbations poleward of 30° latitude. The small scale initial perturbations which tend to be the most rapidly growing are taken from the leading singular vectors of the first 48 hours in the forecast. And to get more slowly growing large scale perturbations the evolved singular vectors from the previous 48 hours are also calculated. By Gaussian sampling 25 perturbations which are then added and subtracted to the analysis, 50 perturbed initial conditions are obtained. The system now consist of 50 perturbed forecast and one unperturbed forecast (the control run), and it is denoted 50+1 members. Since the calculation of the singular vectors is quite costly, they are run with a horizontal resolution of T42 and 31 vertical levels and with simplified physics, and they are computed separately over the northern and southern hemispheres, as well as over parts of the Tropics.

The application of singular vectors only account for uncertainty in the initial conditions. But to simulate model errors due to parameterized physical processes, the EPS at ECMWF also employs stochastic physics. This is done by adding an extra stochastic forcing term to the parameterized physical processes on all the members, except the control run (Buizza et al., 1999).

The EPS at ECMWF has since 2006 been run with T399 (50km) and 62 levels, and provides a forecast for up to 10 days. The main purpose with the EPS is to bring additional value to the deterministic forecast, forecast the predictability of the day and in addition forecast the probability of different weather events. The latter is important for extreme weather events, which may cause damages and risks to human life and property. Since extreme weather is rare by nature, a probabilistic approach is more appropriate.

2.2 Dynamical Downscaling

Global models have too coarse resolution for resolving mesoscale and finer features. To be able to study sub-synoptic scales over an area of interests, a small domain with high resolution is nested inside a coarser global/regional model (e.g. Laprise et al., 2000; Xue et al., 2007; Branković et al., 2008). The fine model is imposed by lateral boundary conditions and initial conditions from the coarser model. This nesting approach is referred to as dynamical downscaling.

In this study the dynamical downscaling of LAMEPS has been done with the UK Met Office Unified Model (UKMO UM) and will be presented in the end of this section. First LAMEPS will be described followed by a closer description of UM. The different model configurations described are taken from the time of the IPY-THORPEX campaign.

2.2.1   LAMEPS

Since the introduction of the EPS at ECMWF it has shown increasingly skill in proba-
bilistic forecasting on the synoptic scale[1]. Nevertheless, the global ensemble prediction
system still employs a too coarse grid mesh to represent meso and smaller scale features.
It is suggested that a finer model resolution will improve this (e.g. Mass et al., 2002).
However, with increasing model resolution, there will be a decrease in error-doubling
time (Lorenz, 1969; Hohenegger and Schär, 2007), and the predictability limit will be
reached earlier in the forecast than for the synoptic scale integrations.

A short range High Resolution Limited Area Model Ensemble Prediction System
(LAMEPS) is thought to enhance the prediction quality on the mesoscale. At met.no
LAMEPS has been run in operationally weather forecasting since 2005, and shows great
skill in capturing different weather situations (Frogner and Iversen, 2002; Frogner et al.,
2006; Jensen et al., 2006). It is run with the Norwegian configuration of the quasi -
hydrostatic limited area model HIRLAM version 7.1.4[2] with a horizontal grid mesh of
$0.108^o \times 0.108^o$ (12 km) and 60 vertical levels. The control run analysis employs the
3D-Var 6-hourly data assimilation cycling. The perturbations to construct the ensem-
ble members are taken from targeted EPS at ECMWF (TEPS) (Frogner and Iversen,
2001). TEPS uses the same model version and set up as EPS described in section 2.1.
However, instead of using 25 singular vectors (SVs) targeted to the northern hemisphere
north of 30°, only 10 SVs are used, and they are targeted to maximize the total energy
within northern Europe and adjacent areas at the final optimization time of 48 hours
(Frogner and Iversen, 2001). Then the perturbation of each TEPS member relative to
the TEPS control, are added and subtracted to the HIRLAM analysis, and in this way
20 perturbed ensemble members are obtained together with the unperturbed HIRLAM
analysis. To take into account errors which may propagate and develop from inaccurate
lateral boundary conditions, both the initial state and the lateral boundary conditions
are perturbed (Frogner et al., 2006). To include model uncertainties, the members in
LAMEPS are run with altering cloud physic schemes.

The systems TEPS and LAMEPS are also combined to form a multimodel EPS, NOR-
LAMEPS, which consists of a system with 40+2 members (40 perturbed runs and 2
control runs). This is a feasible method to obtain a new EPS without performing any
new runs, and it is another way of including model uncertainties. Even though the two
systems are not completely independent from each other, the ensemble spread is larger
than for both systems alone (Frogner et al., 2006).

2.2.2   UM

The Unified Model (UM) was introduced into operational weather forecasting at UK
Met Office (UKMO) in 1991 and has since been under continuously development. In
2004 met.no started to routinely employ UM. In this study, version 6.1 of UM has been

---

[1]See ECMWF verification scores:
$http : //www.ecmwf.int/publications/library/ecpublications/\_pdf/tm/501 - 600/tm578.pdf$
[2]See $https : //hirlam.org/trac/wiki/ReleaseNotes7.1.4\#Releasenotes of HIRLAM7.1.4$

used and was configured with a 4 km horizontal grid spacing, 38 levels and an integration time step of 100s. These configurations are the same as used for operational weather forecasting at met.no.

When utilizing UM for limited area modeling (LAM), the model runs on a rotated latitude longitude horizontal grid, where the computational North Pole is moved away from the geographical North Pole. This allows the domain to take the advantage of the even grid spacing over equatorial regions. Here the domains are run with the same rotation used in HIRLAM, where the rotated spherical pole is located over Greenland with the coordinates 68°N and 320°E.

In UM the non-hydrostatic equations are solved for the motion on a rotated almost spherical planet, which takes into account the curvature of the earth, and describe the time evolution of the atmosphere. Since the governing equations are non-hydrostatic, where vertical acceleration is allowed, UM is dynamically well suited for very high horizontal resolution modeling (UK Met Office, 2004). In addition, the equations depend on the deep-atmosphere dynamics, which requires that deep-convection is explicitly resolved and shallow convection parameterized. The definition of deep and shallow convection depend on the amount of the convective available potential energy (CAPE: an expression for the energy available to form deep convection), in each grid box.

The variables used in UM are computed every time-step and in each grid point, and the primary prognostic variables include the horizontal wind (u and v), vertical wind component (w), potential temperature (θ), Exner pressure (Π), density (ρ) and components of moisture (vapor, cloud water and cloud ice) (UK Met Office, 2004). To solve these equations, a semi-implicit, semi-Lagrangian, predictor-corrector[3] scheme is used. In the horizontal the equations are solved with Arakawa-C grid point scheme, and in the vertical the Charney-Philps grid scheme is used (Staniforth et al., 2002). The Charney-Philps grid scheme follows the terrain near the surface and turns constant higher up. The 13 first levels are below 3 km, where level 1 is approximately at 20 m and level 38 is 65 km up in the atmosphere. The grids have a staggered structure in all directions, and the particular grid type has either integral or half integral values, i.e. P or P$\pm$1/2, where P is either i, j, k in the models physical space. Figure 2.2a shows the horizontal arrangement of the primary variables u, v, and Π on the vertical level $k = K \pm 1/2$, where u and v are on the same vertical level as Π, but on different horizontal grid points. Figure 2.2b shows the arrangement of the vertical grid structure relative to the top and bottom boundaries. The horizontal velocity is on the same level as Π, and θ and moisture variables are on the same level as vertical velocity.

Atmospheric processes that operate on a smaller scale than the horizontal grid mesh cannot be resolved and are therefore parameterized. These physical processes may include boundary layer turbulence, convection, large scale cloud scheme, radiation and subsurface, surface and layer processes. In UM all of these processes include a com-

---

[3]The predictor step approximate the non-linear terms in all processes, and in the end the correction step update the approximated terms to achieve most accurate solutions.
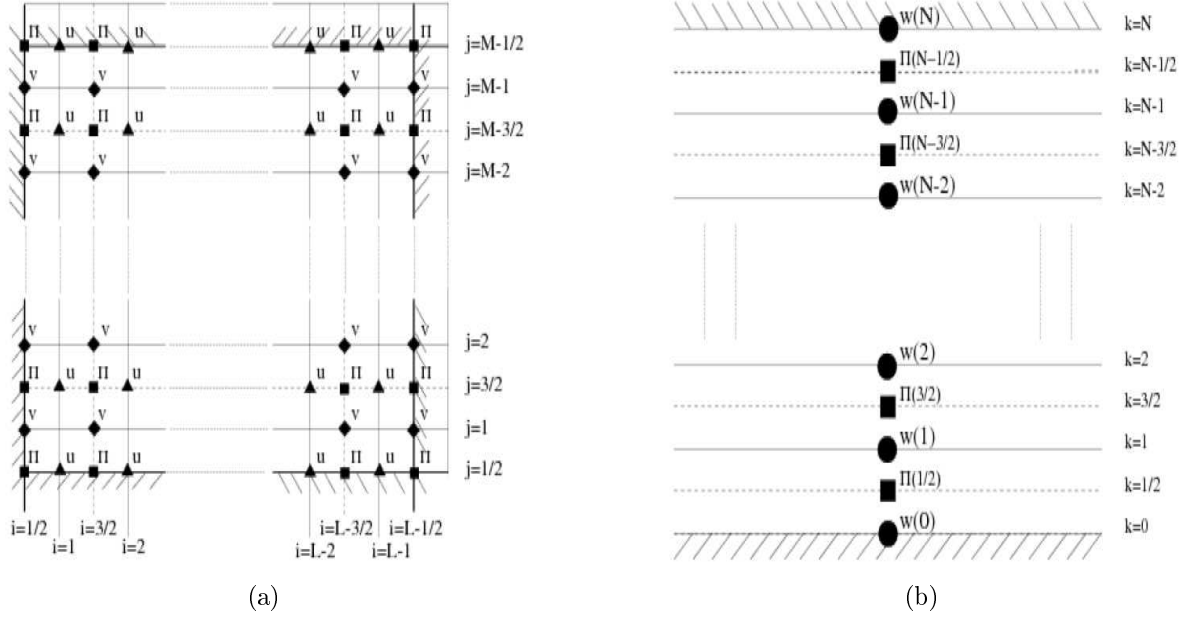
Figure 2.2: *(a) shows the horizontal grid structure, and (b) shows the vertical grid structure in UM. Figure adapted from Staniforth et al. (2002)*

prehensive set of parametrization, and they are listed in Appendix A. The standard configuration at met.no includes an enhanced vertical mixing in the stable boundary layer (SBL), as a result of the unresolved heterogeneity (i.e. orography, land use) at the surface. In this study we wanted to further investigate the sensitivity to the physics representing the SBL. Therefore additional experiments was performed with less vertical mixing in the stable boundary layer. A closer description of the parameterization of the SBL is also found in Appendix A.

2.2.3   Downscaling LAMEPS with UM

In this experiment we have downscaled LAMEPS with UM. The reason for downscaling LAMEPS instead of NORLAMEPS is based on the fact that it was a too big jump to go from T399 (50 km) to 4 km instead of 12 km to 4 km. Each LAMEPS member provided initial conditions and lateral boundary conditions to UM, and this gave an ensemble of UM runs. The LBCs were imposed each hour during the forecast. The rim width[4] was set to 8 grid points. This was used as recommended from UKMO, and in this study we have not investigated the sensitivity to the rim width.

The downscaled ensemble system consists of 20 + 1 member (one being the control run), called UM-EPS. For this purpose we have set up two new domains, one with 300

---

[4]Rim width is the with of the region around the edge of the domain that will undergo a weighted relaxation back to the values in the LBC fields. If there is a large rim width, there will be a smooth relaxation, however, the area of the domain to run free is reduced.
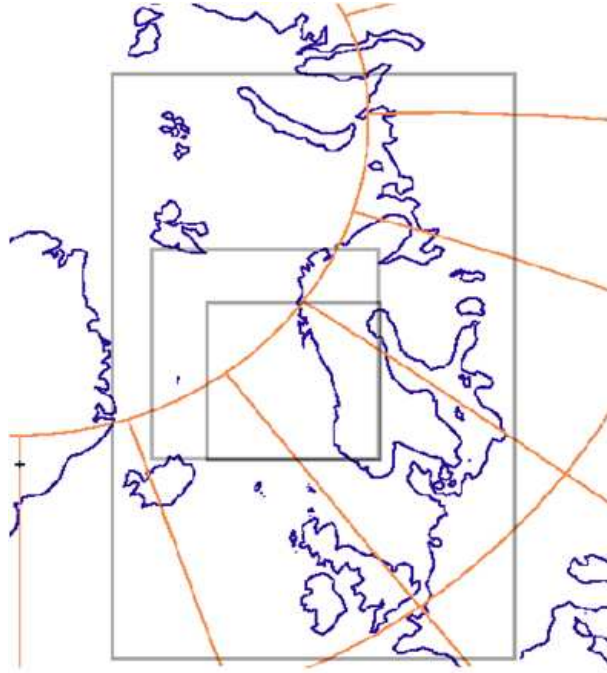
Figure 2.3: *The different domains used in the experiments. The outer domain is the HIRLAM domain used in LAMEPS. The two domains inside are the new domains set up for the UM-EPS, one with 390 × 490 grid points, and the other one with 300 × 300 grid points. They are called UM-EPS-big and UM-EPS-small, respectively. The HIRLAM domain has a horizontal grid mesh of 12 km, and the two UM domains both have a 4 km horizontal resolution.*

× 300 grid points and the other one with 390 × 490 grid points, and the domains are showed in Figure 2.3. The largest domain is called UM-EPS-big and the smaller one UM-EPS-small. The location of the domains was determined by the development of the polar low from the IPY-THORPEX campaign. The main purpose of performing the forecast on two integration domains was to see how the integration size affect the prediction.

The forecasts LAMEPS, UM-EPS-small and big are all initialized 18 UTC 02.03.08 and are run for 60 hours. Also, since there was an enhanced observation network during the IPY-THORPEX campaign, these observations are assimilated into the LAMEPS forecast. The extra campaign data consists of the drop sondes from the aircraft, radiosondes from the different coastguard ships, Bear Island, Novaja Semlja, Murmansk and Franz Josefs.

2.3   Polar lows

A rapid change of the wind direction, an increase of the wind strength, and heavy precipitation can be a warning of the approach of a polar low. Throughout history many fishing boats have shipwrecked due to the sudden approach of the strong wind, which forecasts have failed to predict. The rapid development over oceans where the observations are sparse, and their small scale render polar lows difficult to forecast, and therefore life and property have been lost. Even though people were aware of these small storms, they were not known to be a common phenomenon until the introduction of satellite images in the 1960s, where the significant cloud structure was detected in the images (Rassmussen and Turner, 2003). It was realized that these phenomena mainly develop during the winter months and over high latitudes. With growing awareness of these weather phenomena, there has been a great interest in them. This has resulted in various studies. To assess polar lows' temporal and spatial distribution there have been different climatological studies (e.g. Harold et al., 1999; Noer and Ovhed, 2003; Kolstad, 2006; Zahn and Storch, 2008; Blechschmidt, 2008). To achieve better understanding of the different physical structures and forcing mechanisms, several case-studies and more theoretical studies have also been performed (e.g. Rasmussen, 1979; Emanuel and Rotunno, 1989; Montgomery and Farrell, 1992; Nordeng and Rasmussen, 1992; Yanase and Niino, 2006).

Polar lows tend to develop during cold air outbreaks. This is when cold arctic air flows from the ice sheet over the ocean. Under these conditions there are large temperature differences between the warmer ocean and the cold over-sweeping air, and the lowest atmospheric layer will be destabilized and yield enhanced convection. The reason for the relatively warm ocean is a Western Boundary Current which brings warm, tropical, saline water up to higher latitudes (Hartmann, 1994). In the Northern Hemisphere (NH) there are two main currents like these, the North Atlantic current (more commonly known as the Gulf Stream), and the Kuroshio current. As a result of these currents the sea surface temperatures (SST) in these areas have a higher temperature when compared to other regions at the same latitude throughout the year. Polar lows are most commonly found in the areas around Svalbard, the Norwegian Sea and in the Barents Sea, but there are frequently observed developments around Greenland and east of Canada, the Beaufort Sea, the Bering Sea, the Northwest Pacific and the Sea of Japan. Polar lows can be found in high latitudes of the Southern Hemisphere (SH) as well, but (possibly due to the colder ocean) they are not as intense as the ones found in NH.

The study of polar lows is still relatively new and therefore the theoretical understanding is not complete. But it is realized that there are many different forcing mechanisms which trigger polar low developments, giving a "polar low spectrum". They may appear as almost purely baroclinic or almost purely convective systems (Rassmussen and Turner, 2003). However, a combination of these two instabilities is most commonly seen. A polar low is thought to develop in a baroclinic atmosphere through an interaction between an upper-level positive potential vorticity (PV) anomaly which moves over a region of strong temperature gradients. The cyclone is growing by converting potential energy from the temperature gradients to kinetic energy through ascending

warm air and descending cold air (Rassmussen and Turner, 2003). The cyclone may continue developing as a baroclinic disturbance, or it may be intensified through thermal instabilities such as the Conditional Instability of Second Kind (CISK) mechanism, or the wind induced surface heat exchange (WISHE) theory. The CISK theory is based on a reservoir of CAPE, and through a cooperative feedback between deep convection and the large scale flow, there may be a slow intensification of the cyclone (Rasmussen, 1979; Bratseth, 1985). The WISHE theory (formerly referred to as air sea interaction instability; ASII) do not require the ambient CAPE to intensify the cyclone, but the high wind speeds induce sensible and latent heat fluxes from the sea surface which is then transported upward by turbulent motions and convection (Emanuel and Rotunno, 1989).

There are different cloud signatures associated with the different forcing mechanisms, where the baroclinic systems are characterized with a comma cloud and the convective systems have a more spiral form shape, often with a cloud free eye. A baroclinic polar low may develop as reverse shear systems where the horizontal wind speed decreased with height, and the thermal wind is opposite in direction to the mean flow. Reverse shear conditions are thought to be important for many polar low developments (Kolstad, 2006). Further, polar lows dissipate very quickly after making landfall, as a result of loosing their energy source. Polar lows are characterized with their relative small scale, and in the Nordic Sea areas the horizontal extent is most commonly from 200 - 500 km (Noer and Ovhed, 2003). Polar lows may bring high impact weather, where there is heavy precipitation and the winds often exceed gale force (14 - 17 m/s). Polar lows are a wintertime phenomenon, with the high frequency season from October to March.

### The observed polar low during the IPY-THORPEX campaign

The International Polar Year (IPY, 2009) lasted from March 2007 to March 2009 and was a collaborative scientific effort among several countries where the focus was on the Arctic and the Antarctic. It was organized through the International Council for Science (ICSU) and the World Meteorological Organization (WMO), and the aim was to improve the understanding in polar regions through enhanced research activity. The IPY-THORPEX campaign (IPY-THORPEX, 2009) was one of the projects during the IPY, and it lasted 3 weeks in February-March 2008. It was founded by the Norwegian Research Council and the main interest was to improve weather forecasting of hazardous weather in the arctic region. During the campaign there were several researchers stationed on Andøya, an island in Northern Norway, and together they analyzed weather charts and satellite images to find where polar lows might develop. A special aircraft equipped with in-situ sensors for basic meteorology and turbulence measurements, and one water vapor and one wind Lidar system in addition to a drop sonde system, flew the routes that the scientists planned the day before, and in this way the observation data were obtained. Along with the measurements from the flights, there was an enhanced observation network during the campaign; where several radiosondes were deployed from different coastguard ships, the Bear Island and also from Novaja Semlja, Murmansks and Franz Josefs where some Russian scientists were also participating. All of these extra data were assimilated into the forecasts aiming to improve them. As a result of
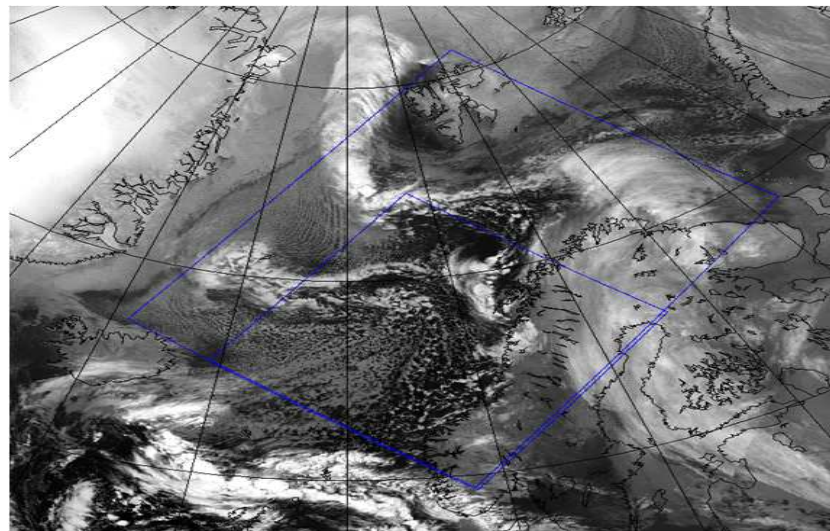
(a)
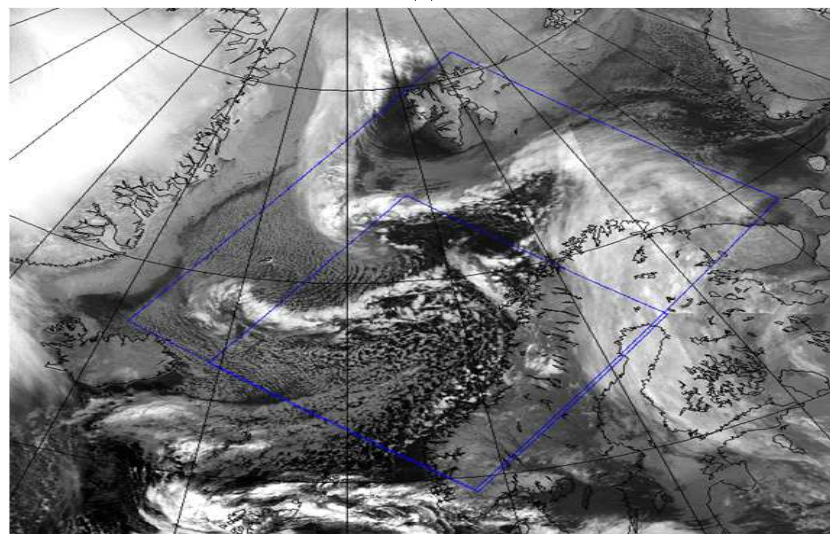
(b)
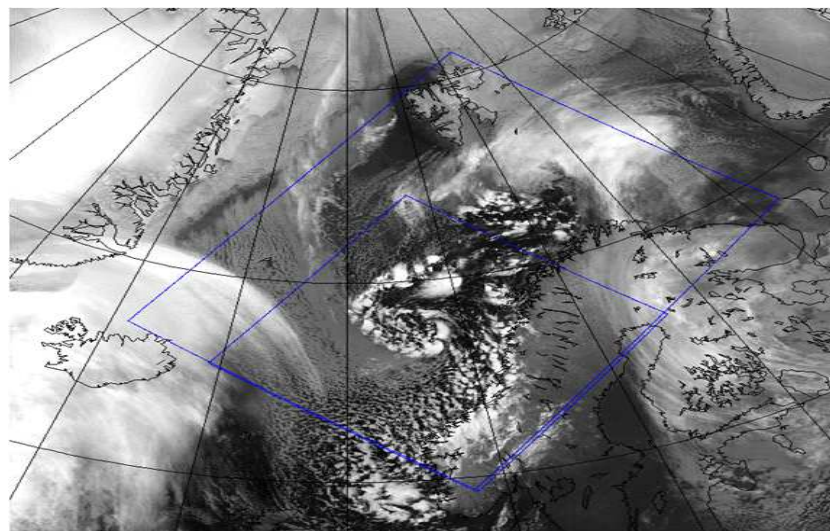
(c)

Figure 2.4: *Satellite images from 11.37 UTC 03.03.08 (a) 17.21 UTC 03.03.08 (b) and 11.28 UTC 04.03.08 (c). The blue squares indicates the domains set up for this study.*
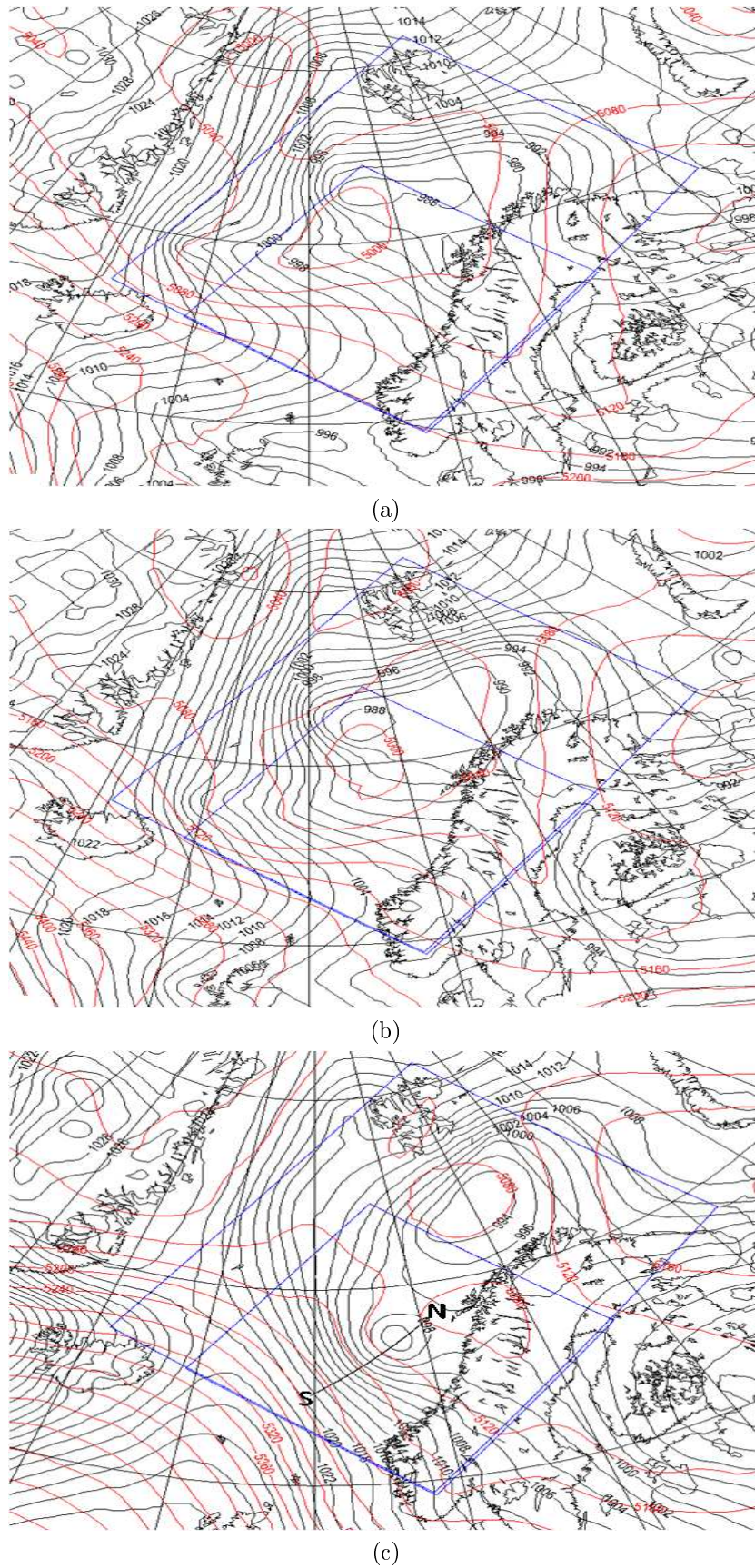
(a)

(b)

(c)

Figure 2.5: *MSLP and Z500 from HIRLAM20 analysis at 12 UTC 03.03.08 (a), 18 UTC 03.03.08 and 12 UTC 04.03.08 (c). The blue squares indicates the domain set up for this study. The isobar interval is 2hPa and 40m for Z500. The line N-S is the location of cross section used in Chapter 4.*

this campaign, the researchers managed to observe and measure a polar low in a way which has never been done before.

From 3 through 4 March 2008 a polar low developed in the Barents and Norwegian Seas, and there were 3 flights in 2 days which measured the entire lifecycle, two flights 03.03 and one flight 04.03. The satellite images from approximately the same time as the flights can be seen in Figure 2.4, where 2.4a shows the first stage of the polar low associated with the cold air outbreak (11.37 UTC 03.03.08), 2.4b the early phase of the cyclone (17.21 UTC 03.03.08), and the secluded cyclone just before it made land fall can be seen in 2.4c (from 11.28 UTC 04.03.08). Figure 2.4 should be seen together with Figure 2.5 which shows the HIRLAM20 (20 km resolution) analysis of MSLP and the geopotential height at 500 hPa, Z500, from 12 UTC 03.03.08, 18 UTC 03.03.08 and 12 UTC 04.03.08, respectively. This polar low was associated with a synoptic low, which was located off the west coast of Norway a couple of days before the polar low development. The synoptic low triggered the cold air outbreak, which is evident in Fig 2.4a, where the cold arctic air flows over the relative warmer ocean forming long rows of stratocumulus (cloud streets). The frontal zone, which separated the shallow, low-level Arctic air masses from the warmer, maritime air over the sea, is also seen in the figure, where it has a north south orientation on the west side of Svalbard. Flight 1 flew over the frontal zone and released several drop sondes. From the observation data (not shown here) a strong low-level, horizontal wind shear across the frontal zone is seen. The wind at 925 hPa was observed to be up to 26.2 m/s. The observation data also show very strong temperature gradients across the frontal zone.

The next stage in the development seen in Figures 2.4b and 2.5b shows the early phase of the polar low. There is still cold advection in the flow from the north and now it is starting to bring the cold air south of the synoptic low and in its initial phase of wrapping in the warm air. There are still strong surface winds on the western flank of the synoptic low, at the same place where the temperature gradients are largest.

Around 00 UTC 04.03 (not shown) a mesoscale vortex cuts off the synoptic low on its west flank, and continues to propagate towards the coast of Norway. Figure 2.4c and 2.5c shows the secluded cyclone just before it made land fall. At this time the polar low had a diameter of approximately 500 km and the HIRLAM20 analysis shows a central pressure of 996 hPa. The cloud bands are spiraling around the low center. For this time the campaign aircraft flew immediately above the core, and from the observation data it is seen that the low level jet has a wind speed up to 28m/s, and it is evident how the cold air has been advected to the north side of the warm core. The polar low made landfall around 18 UTC and died out as a result of the lack of energy from the warm ocean.

One of the great paradoxes during this campaign was the use of forecasts which the scientists believed to have bad skill in predicting polar low events. They still had to use them to analyze when and where a polar low might develop. Sunday 02.03 the researchers realized they missed a polar low which hit the middle of the Norwegian

coast the same day. Fortunately the same day they predicted a polar low to develop during the next day and to hit the middle of Norway on Tuesday morning. The deterministic HIRLAM20 forecast initialized 18 UTC 02.03.08 predicted the large scale flow with good accuracy during the whole forecast, but the smaller scale, and especially the observed polar, low was not captured. The first forecast which had the polar low was the HIRLAM20 forecast initialized 00 UTC 03.03.08 (Monday), but it predicted the polar low to make landfall a few hours earlier than actually occurred. The skill in predicting the polar low increased with initializing time closer to the polar low event, and the forecasts initialized on 12 UTC 03.03.08 and beyond have the right strength and location of the observed polar low.

Chapter 3

Verification Methodology

3.1 Standard Methodology

The observation data from the campaign used in this study consists of wind speed at 925 hPa, in addition to vertical cross sections of wind speed and potential temperature. The vertical cross sections are interpolated from the observations from the drop sondes. During the three flights there were several drop sondes released, but for this purpose we have only chosen one cross section from flight 3 to compare with and the geographical position can be seen in Figure 2.5c. Regular satellite images (Fig. 2.4) and radar reflectivity (Fig. 4.9a and b) will also be used to compare with the forecasts in addition to the HIRLAM20 analysis shown in Figure 2.5 and QuikSCAT[1] (not shown). The standard analysis tools at met.no have been used to calculate the mean sea level pressure (MSLP) ensemble mean and the spread (σ) of the systems, in addition to the different forecast probabilities of wind, precipitation and potential temperature. The ensemble mean is given by:

$$\overline{x} = \frac{1}{n} \sum_{i=1}^{n} x_i,$$

where n is number of ensemble members (including the control) and x_i is the grid point value of x for ensemble member i. A measure of the spread between the members is given as the root mean square (RMS) deviation from $\overline{x}$:

$$\sigma = \sqrt{\frac{1}{n} \sum_{i=1}^{n} (x_i - \overline{x})^2}.$$

By taking the mean we are filtering out the unpredictable parts in the flow. The small scale is the most unpredictable part in the flow where the errors are first saturated, therefore with the ensemble mean the small scales are first filtered out. As a result of increasing lead time the ensemble mean will gradually become smoother and only retain the large scale which is more predictable. The ensemble mean is expected to be as good as the control run in the early range of the forecast, but become more skillful thereafter. σ is an indication of the skill of the ensemble mean. When σ is small, it is small spread

---

[1]QuikSCAT definition: High-resolution satellite-derived ocean surface wind.

between the members, and the ensemble mean is expected to be skillful. Large spread between the members is an indication of a less predictable regime, and the ensemble mean (or the control run) is not expected to be skillful (but can be lucky).

The probability thresholds have been chosen with respect to the observations, and the probability is given in percentage, where 100% (0%) means that all the members (none) exceeds the threshold. As discussed in section 2.1, the forecast probability of different weather events is highly important especially when it comes to high impact weather. Probabilistic forecasting can increase the warning ahead of an incident to a larger extent than what a deterministic forecast is capable of. In addition, probabilistic forecasting is a more consistent way of forecasting than a deterministic forecast.

In this study we have chosen 3 verification times where the model results are compared against the observations. Since the flights lasted over several hours, the lead time has been chosen with the goal to be as close as possible to the flight time. The verification times are listed in Table 3.1.

Table 3.1: *The verification times of the model results against the observation data.*

Flight time	Verification time	Lead time
Flight 1: 10.09 - 13.58 UTC →	12 UTC 03.03.08	T+18h
Flight 2: 14.56 - 18.26 UTC →	18 UTC 03.03.08	T+24h
Flight 3: 10.14 - 13.28 UTC →	12 UTC 04.03.08	T+42h

Furthermore, in this experiment two new methods to analyze the forecasts have been taken into use; pseudo satellite images and tracking of polar lows. These two methods will be described in the following.

3.2 New Methods

3.2.1 Pseudo satellite images

Satellite images of cloud top temperatures are of great importance for visual inspection and understanding of the evolution of weather systems. It is an important analysis tool, especially in data-sparse areas, for short range weather forecasting, helping to define the initial conditions to initialize numerical weather predictions models (NWP), and also monitoring NWP model performance in the early stage of the forecasts (Bader et al., 1995). Moreover, satellite images are also important for polar low forecasting, since these features are easily detected in the images. In addition, many studies related to polar lows have benefited from the satellite observations (e.g. Harold et al., 1999; Blechschmidt, 2008). Since a satellite imagery gives such good understanding of the different parameters and the 3D structure of the weather system, it is desirable to obtain similar images from model forecasts. Also, the quality of various model fields can be estimated by comparing with observations, while in data-sparse areas a judgment of the quality

can only be made on the basis of satellite images (Tijm, 2004). Therefore a calculated satellite image from model forecasts simplifies the assessment of the different parameters, especially in data-sparse areas.

Tijm (2004) proposed a simple and quick method that estimates both infrared (IR) and water vapor (WV) pseudo satellite images based on HIRLAM model forecasts. The term pseudo is used to indicate that these images are based on model derived fields rather than remotely sensed radiation. These pseudo satellite images are analogs to conventional IR and WV images. The conventional IR imagery is derived from terrestrial radiation emitted in the 10 - 12 μm wavelength band region. WV imagery is derived from the radiation emitted by water vapor at wavelengths in the 6 - 7 μm region (Bader et al., 1995).

We have here in this study adapted the method developed by Tijm (2004) such that pseudo satellite images can be obtained from UM forecasts as well as HIRLAM. We have mainly been focusing on the pseudo satellite IR images, therefore only these will be presented here. In the following first a brief presentation of the pseudo satellite images method and associated model variables used in the algorithm will be given. The sensitivity to some of the parameters have been investigated, and the algorithm has been verified using the control run of UM-EPS-big in addition to a UM4 (4 km) operational forecast from met.no. This was done for two purposes: (1) The method was developed before all the runs in this study was done, and (2) it gives a larger confidence in the method if it is verified with more than one case. The operational domain is mainly located over land in contradiction to the experimental domain which is mainly over ocean. The forecast from the operational domain is initialized 12 UTC 16 March 2009. The initial and lateral boundary conditions are taken from HIRLAM8 (8 km) forecast. Besides from this, the model configurations are the same for both domains, and is described in section 2.2.2.

The method

Whereas the satellite retrieved cloud top temperatures (CTTs) are inverted from the remotely measured upwelling radiation at the top of the atmosphere, the model derived pseudo satellite images estimate the cloud top temperature by using temperature, pressure and cloud and ice water content (Tijm, 2004). We integrate starting at the surface using the surface radiation temperature. In clear sky conditions this temperature corresponds to the CTT in the pseudo image. In cloudy conditions the radiation temperature of each model layer is set equal to the associated model temperature. However, its contribution to CTT is dependent on the amount of cloud condensate (liquid and ice) in the layer. If the amount exceeds a certain threshold (see below), the model cloud layer radiates as a blackbody.

The cloud top temperature in the IR wavelength band is calculated with the equation:

$$T_{cld} = T_{cld,prev}\left(1 - MIN\left\{1, \frac{Q_l \Delta P}{Q_{dp}}\right\}\right) + T_a\left(MIN\left\{1, \frac{Q_l \Delta P}{Q_{dp}}\right\}\right), \qquad (3.1)$$

where T_{cld} is the cloud top temperature (in K) at the current model level and $T_{cld,prev}$ is the cloud top temperature at the previous model level. Q_l is the sum of the mean grid box cloud and ice water content at the current level (kg of condensate per kg of air), ΔP is the pressure difference between adjacent model levels (in Pa), i.e. the thickness of the model layers, T_a is the model temperature of the current level and Q_{dp} is the aforementioned threshold value. The threshold Q_{dp} is currently set to 0.5 ($\frac{kg}{m^2}$), same as in Tijm (2004). From the hydrostatic equation it can easily be seen that $Q_l\Delta P$ is proportional to the cloud condensate content per square meter in the column with height. Note that this method is derived for HIRLAM, which is a quasi-hydrostatic model. UM is a non-hydrostatic model, but by adapting this method even though it is based on hydrostatic assumptions has not affected the results (see the following).

Starting at the surface and moving upwards, Eq. 3.1 is solved for each layer. If there are no cloud or ice water content in the layer, i.e. Q_l=0, the CTT remains the temperature of the previous cloud layer. If there are cloud or ice water content present, the CTT is adjusted to the temperature of that level, where the ratio $\frac{Q_l\Delta P}{Q_{dp}}$ determines how much the CTT should be adjusted to the temperature of the current layer. For values larger than 1, the cloud layer behaves as a blackbody.

The grid box mean cloud and ice water content are prognostic variables readily available on the full-levels in UM. Potential temperature, from which the temperature used in Eq. 3.1 is derived, is also given on the full-levels. In order to save disk space and avoid having too large output files, pressure is currently only archived at the half-levels, and therefore is interpolated to the full levels for both the calculation of temperature and pressure difference in Eq. 3.1.

Note that CTT of Eq. 3.1 will most likely depend on the number of vertical levels employed in the model. In this study we have not investigated the sensitivity to the number of vertical levels.

Results

Pseudo satellite images are in operational use at met.no for only HIRLAM12 forecasts, and hence only these are used here for comparison to the UM4 forecasts. HIRLAM12 has a 12 km horizontal grid mesh and 60 vertical levels. In addition, satellite images closest in time are used for verification.

Both the satellite and model derived pseudo satellite images are displayed here using the graphical visualization tool DIANA. Similar to the conventional satellite images, the whiter (darker) area in the pseudo satellite image, the lower (higher) is the CTT. However, the black to white scaling is dynamic, i.e. the highest (lowest) CTTs within the model domain will be displayed darkest (whitest). Since we are mainly interested in the spatial gradients in CTT, this dynamic scaling is sufficient for differentiating between high and low clouds in the model. However, for a more detailed comparison it is desirable that the pseudo satellite images are tuned to the CTTs of the satellite images.

(a)   (b)   (c)
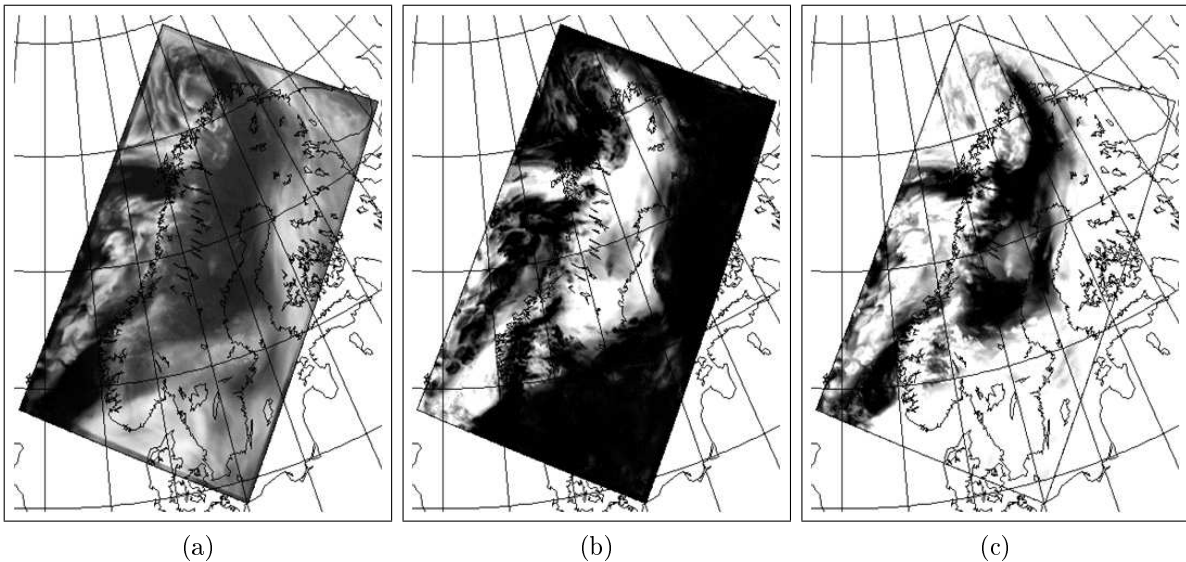
Figure 3.1: *Pseudo satellite image (a) compared against the UM total cloud cover (b) and inverted total cloud cover (c). The high coluds are seen to the south and north-east in the domains, and cloud free regions are found in the middle of the domains. Lower and middle level clouds are seen to the north west and west. See text for further details.*

This will mainly affect the CTTs where there are clouds, since the CTT over ocean and land where there are no clouds and, to some extent, coincide well with the observed dark color (see the following).

Sensitivity tests

We have investigated the sensitivity of some of the parameters used in the algorithm. Since the pressure field is interpolated from half to full levels, we wanted to investigate the sensitivity of this interpolation. The CTT image was calculated using pressure at both half and full levels with the control run from UM-EPS-big (not shown). There were no differences detected by visual inspections, therefore we conclude that our interpolation of pressure from half - to full - levels is sufficiently accurate for the calculation of CTT in Eq. 3.1.

The surface radiation temperature in HIRLAM is the near surface temperature (T2m). In UM there is a diagnostic surface temperature, Ts, which is at 0 m and will therefore better represent the surface radiation temperature. To see if using T2m instead of Ts gives significant differences, we also estimated CTT by using Ts with the operational UM4 forecast (not shown). As expected the sensitivity to the choice of lower boundary temperature (T2m or Ts) is not very large. Hence, we decided to replace T2m with Ts in Eq. 3.1.

Comparing with the diagnostic total cloud cover in UM

Having decided on using interpolated pressure fields and Ts in Eq. 3.1, we next compare the pseudo images to the modeled diagnostic total cloud cover, seen in Figure 3.1. We use the operational UM4 forecast, same as in the above subsection. For the total cloud cover image (Figure 3.1b), white areas (i.e. areas without any shading) are indicative of cloud free grid regions, whereas the darker the grid box the larger the cloud cover. Obviously, this is opposite to how it is seen in the satellite images, and can as a consequence easily be confused. We have therefore also inverted the shading, Figure 3.1c. The advantage of using pseudo satellite images instead of total cloud cover is evident. For instance, in the pseudo satellite image one can distinguish between high and low clouds. Nevertheless, the clouds in the pseudo satellite image are co-located with the total cloud cover. Hence, we are confident that Eq. 3.1 is able to detect the modeled clouds.

Comparing with satellite IR images and HIRLAM pseudo satellite images

Pseudo images are calculated from the operational UM4 and HIRLAM12 forecasts initialized at 12 UTC 16 March 2009. Two forecast lead times, T + 6h (afternoon) and T + 18h (early morning), are shown in Figure 3.2. The corresponding satellite IR images seen in Figs. 3.2 a and b are used for verification.

First we compare the UM4 images with the satellite IR images. At lead time T + 6h, the same features seen in the observed image also appear in the pseudo satellite image. The high clouds south - east and north - east in the UM4 domain, correspond to what is observed. There are more differences comparing these two images west in the UM4 domain, along the Norwegian coast. There are middle level clouds forecasted, consistent with IR-images. Thus the amount of clouds forecasted is less than observed. Both images have clear sky conditions east in Northern - Norway and Sweden. However, the surface radiation temperature over land where there are no clouds in UM appears darker then to the observed, and this is also the case for the radiation temperature in cloud free areas over ocean. At lead time T + 18h, the same characters in both images are still seen. It is striking how well the clouds in the pseudo satellite image are co-located with the satellite image. Though, there are fewer clouds in the pseudo satellite image than what is observed. But overall the pseudo satellite images in UM coincide well with the observed satellite images.

Having seen that the UM4 pseudo images compare well with the satellite images, we next compare them to the HIRLAM12 images. Remember that the pseudo method was originally developed for HIRLAM (Tijm, 2004). Due to the coarse grid mesh in HIRLAM12 the CTT field is smoother and the range in the CTT values is not as large as in the satellite IR image or the UM4 image. Also, UM4 shows more distinct differences between ocean and land, and more detailed structures appear. This is due both to the higher horizontal resolution and the fact that HIRLAM uses T2m. Generally, pseudo satellite images from UM resemble the observed satellite images more than HIRLAM
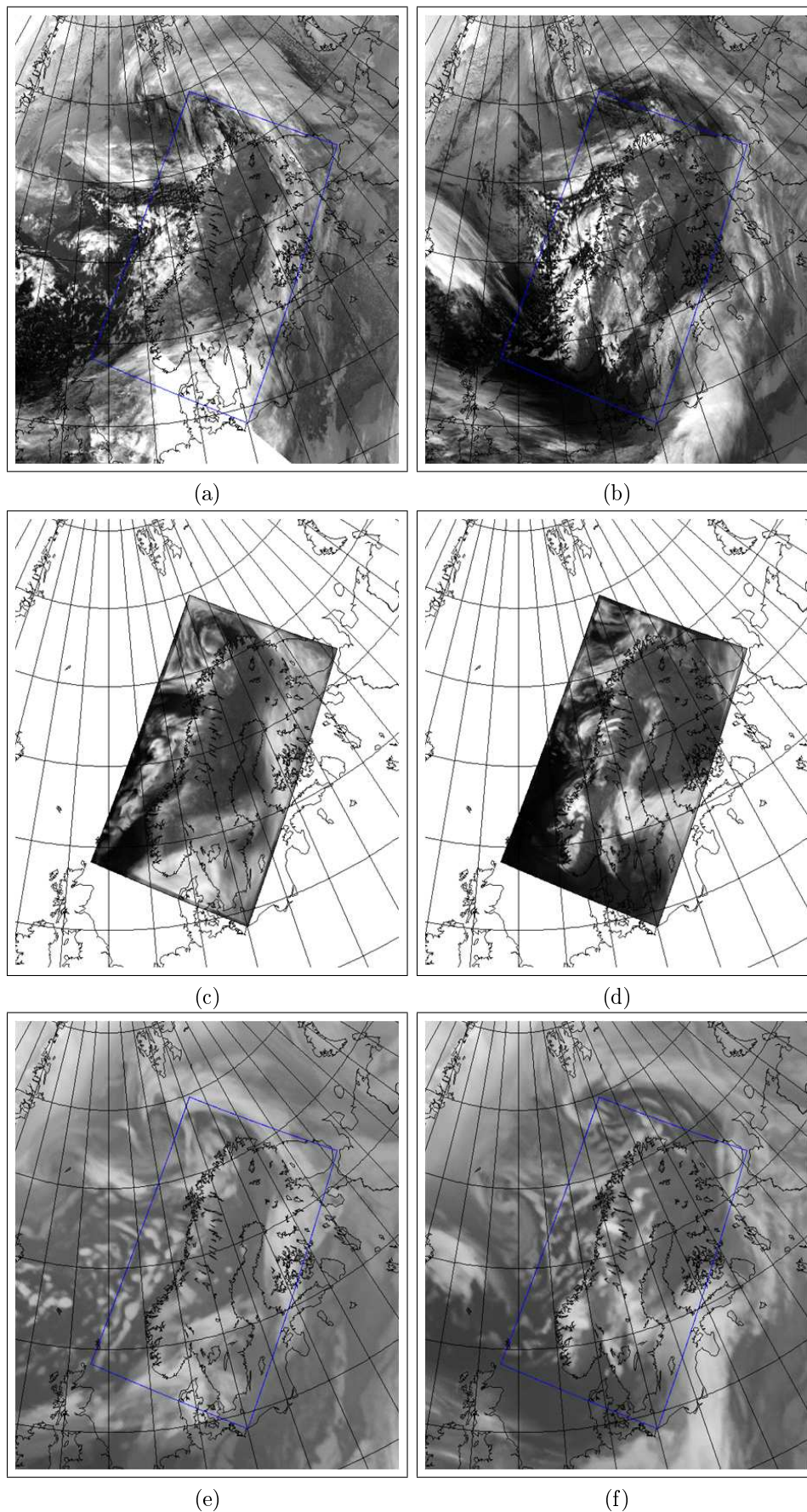
Figure 3.2: *IR satellite images and pseudo satellite images from UM4 and HIRLAM12. The forecasts were initialized at 12 UTC on 16 March 2009. The IR satellite images are valid at 1808 UTC 16 March 2009 (a) and 0600 UTC 17 March 2009 (b). Pseudo satellite images at lead time T + 6h from UM4 (c) and HIRLAM12 (e), and at T + 18h from UM4 (d) and HIRLAM12 (f). For convenience the UM4 domain is shown in the IR and HIRLAM12 pseudo satellite images (the blue squares).*

pseudo satellite images.

The use of pseudo satellite images in this study

Since clouds are a product of all processes in the atmosphere, the pseudo satellite images
gives a good understanding of the 3D structure of the weather systems in the model.
In addition, these images give a direct judgment of the quality of various model pa-
rameters, especially in data - sparse areas. In this study we will calculate the pseudo
satellite images on the outputs from UM-EPS and compare them with satellite images
(presented in Chapter 4).

3.2.2   Tracking polar lows

For polar low forecasting, as well as detecting the "real world" cyclones, it is important
to exclude falsely identified phenomena in model outputs. Several previous studies have
applied a tracking algorithm (e.g. Hodges, 1994, 1995, 1999) on different model fields
based on an automated method to identify synoptic systems and provide statistical in-
formation about their positions, intensities and the genesis and lysis (the spatial and
temporal distribution of the development and the ending of the cyclone) (e.g. Hoskins
and Hodges, 2002; Froude et al., 2007a,b). Note that the term track here refers to
the trajectory of an individual storm, rather than the average track of many storms
(Froude et al., 2007a). The tracking technique is an essential forecast validation tool,
and it gives direct information about the model's ability to predict polar lows (Zahn
and Storch, 2008).

In the same manner as tracking synoptic systems it would give valuable information to
track polar lows. For instance, Zahn and Storch (2008) have employed a near isotropic
bandpass filter to extract mesoscale parts of the MSLP fields from a two year long
simulations with CLM (a climate version of the Local Model of the German Weather
Service), and a tracking methodology has been applied on the fields, aiming to repro-
duce the climatology of polar lows over a two year long simulation. After performing the
tracking algorithm, there were too many detected tracks. However, introducing several
objective criteria, the number of the detected polar lows decreased.

In this study we have employed and modified the tracking algorithm developed by
Hodges (1994, 1995, 1999) for tracking polar lows instead of synoptic scale systems.
The model fields are taken from UM-EPS, aiming to reproduce the track of the ob-
served polar low that developed during the IPY-THORPEX campaign. Some additional
constraints have been introduced since this method was originally made for detecting
synoptic systems. First the method TRACK will be presented, and then the modifi-
cations applied will be described. In addition, further objective criteria adapted from
the study of Zahn and Storch (2008) are presented. It should be mentioned that with
the diagnosis from TRACK, broad statistical information about the detected tracks are
obtained, and only a small part is investigated here. To fully utilize this analysis tool,
it should be performed on several cases.

The tracking algorithm

Historically, there have been two basic approaches to diagnose storm tracks, an Eulerian approach and a Langrangian feature point tracking. Since the beginning of super computers the Eulerian approach has been the convenient way to compute simple statistics from NWPs at a set of grid point with a frequency band representative of synoptic timescales (Hodges, 1999; Hoskins and Hodges, 2002; Anderson et al., 2003). The Langrangian feature tracking approach has been used since the end of the nineteen century, and the early studies were based on manual analysis using daily synoptic charts. With the introduction of NWP models the approach has been advanced further and objective, automated methods have been adopted. This provides good statistical information that describes the storm track activity of the synoptic system (Hodges, 1994; Hoskins and Hodges, 2002). A feature tracking algorithm developed by Hodges (1994, 1995, 1999) has been used extensively in several studies (e.g. Hoskins and Hodges, 2002, 2005; Froude et al., 2007a,b), aiming to track synoptic systems, and to compute their statistical properties and climatology and assess forecast skill and predictability of different models. The tracking algorithm has been adapted into this study to track polar lows, which are of sub-synoptic scales.

The basis of the method is to search for maxima or minima in meteorological fields, and a range of fields can be used; MSLP, geopotential at pressure surface e.g. 500 hPa (Z500), meridional wind (v), temperature (T), potential temperature (θ), vertical velocity (w), relative vorticity (ζ) and potential vorticity (PV). Most commonly the algorithm has been performed on the MSLP and vorticity fields, and only these will be considered here. The choice of the field should be done on the basis of what scale is to be tracked. MSLP is distinctly influenced by strong background flow, and large spatial scales and relative slower moving systems dominate. This yields MSLP field a better choice to track larger scales. ζ is less influenced by the strong background flow and therefore tend to be a better field for identifying smaller scales. However, there are some disadvantages with employing MSLP and ζ. In high-resolution data the vorticity field can be very noisy. Since MSLP is an extrapolated field, the field may be sensitive to how the extrapolation is performed, and also to the representation of the orography in the model (Hoskins and Hodges, 2002).

Assume we have chosen one of the meteorological fields for tracking. Before performing the algorithm, the background flow is removed to only retain the mesoscale part. This is done by first performing a spectral spatial filtering. The field is then represented by a spherical harmonic expansion and the smallest and large spatial scales can be removed (Anderson et al., 2003). The result is a filtered field with spatial scales representative of polar lows. Then the tracking algorithm is performed on the filtered field. The first step in the algorithm is the determination of feature points, which are the positions of the extrema in the chosen field. The next step in the method is to determine the correspondence between the feature points, and the aim is to find the set of tracks that maximizes the smoothness of the trajectories. This is done by minimizing a cost function (Hodges, 1994, 1995, 1999). The detected feature points are then constrained to have a minimum horizontal displacement distance over a given time frame (the lifetime), and in addition

for the vorticity field a given threshold needs to be exceeded. The feature points that fulfill the requirements are linked together and give a trajectory. Now the tracks with their respective statistical information are stored in a record, and it is up to the user to interpret the track diagnosis. The algorithm makes use of these criteria related to the minimum horizontal displacement, the lifetime and the vorticity threshold and can be chosen. These will be discussed in the following.

The tracking algorithm adopted to this study

The tracking algorithm developed by Hodges (1994, 1995, 1999) has been performed on the forecasts made by UM-EPS, and the results will be given in Chapter 4. Here the different aspects investigated before deciding on the final criteria to detect and track the polar low described in section 2.3 will be presented. All the tests have been performed on the control run of UM-EPS-small. In this study we have mainly chosen to perform the tracking algorithm on the vorticity field, but a few tests were also done on the MSLP field. A summary is given in Table 3.2. When performing the tracking algorithm, a search of maximum in the vorticity field and a minimum in the MSLP field is done. This will result in too many detected points due to many small scale local maximum and minimum. To pick out the track of the features representative of polar lows, additional constraints are needed. This is first done by a minimum horizontal displacement distance (from the first detected point to the last detected point) over a minimum lifetime. At first the minimum displacement was set to 10° (approximately 1000 km). Polar lows can be stationary or have a very slow southward motion, so this criterion was switched off. The minimum lifetime was originally set to 24 hours. This constraint is a bit more complex, especially for limited area forecasting. A polar low which already has excised for a while outside the domain and is entering the domain on the lateral boundaries, will be excluded with a too long life time constrain. Polar lows tend to exist for at least 12 hours, therefore we decided to set the minimum lifetime to 12 hours. All the tests in Table 3.2 have zero minimum horizontal displacement and a minimum lifetime of 12 hours. Below is given a presentation of the different testes done.

In previous studies when the tracking algorithm has been used to detect synoptic systems, planetary scales with total wave number less than or equal to 5 have been filtered out (Froude et al., 2007a; Hoskins and Hodges, 2002, 2005). Since polar lows are mesoscale features, and can have a diameter up to 1000 km, we initially removed scales between 200 and 1000 km, but this gave too many tracks. In the study of Zahn and Storch (2008) a filtering of 200 - 600 km was used, and we decided to use the same.

The removal of the background state was investigated in Anderson et al. (2003) where the sensitivity to the spectral spatial filter was explored. They increased the number of total wave numbers removed on the MSLP field, from 5 to 7 to 10. With the removal of 10 wave numbers, the nature of the synoptic feature started to deteriorate. From Test 14 (200 - 1000 km) and 15 (200 - 600 km) in Table 3.2 we see that when decreasing the filtering interval on the MSLP field there is an increase in number of tracks, from 6 (200 - 1000 km) to 9 (200 - 600 km), which is in agreement with Anderson et al. (2003). The

Table 3.2: *The different test performed on the chosen field with the tracking algorithm. All the tests have 0 in minimum horizontal displacement and a minimum lifetime of 12 h. The detected tracks are the tracks after the vorticity threshold and filtering interval constraint.*

Test nr	Field	Threshold $[s^{-1}]$	Filtering [km]	Detected Tracks
1	VOR850	2×10^{-5}	200-1000	11
2	VOR850	1×10^{-5}	200-1000	14
3	VOR850	1×10^{-6}	200-1000	14
4	VOR850	1×10^{-4}	200-1000	4
5	VOR850	1×10^{-4}	200-600	3
6	VOR850	1×10^{-5}	200-600	20
7	VOR850	2×10^{-5}	200-600	20
8	VOR925	2×10^{-5}	200-1000	8
9	VOR925	1×10^{-5}	200-1000	11
10	VOR925	1×10^{-4}	200-1000	6
11	VOR925	1×10^{-4}	200-600	3
12	VOR925	1×10^{-5}	200-600	16
13	VOR925	2×10^{-5}	200-600	16
14	MSLP		200-1000	6
15	MSLP		200-600	9

same is seen for the vorticity field when there is a low vorticity threshold (the vorticity threshold will be discussed later). Decreasing the filtering interval from 200-1000 km (Test 1, 2, 8, 9) to 200 - 600 km (Test 6, 7, 12, 13) the number of tracks increases. When there is a high vorticity threshold, reducing the filtering interval from 200 - 1000 km (Test 4, 10) to 200 - 600 km (Test 5, 11) the number of tracks decreases. This indicates that with a low vorticity threshold, the field is more influenced by larger scales, and is therefore more sensitive to the filtering interval. This gives confidence in choosing the vorticity field with a high vorticity threshold and a narrower filtering interval to perform the tracking algorithm on, since it is less sensitive to the removal of the background state and also better suited for detecting smaller scale system than MSLP. Therefore in this study we will perform the spectral spatial filtering on the vorticity field with a filtering of 200 - 600 km.

Initially, the tracking was performed on vorticity at 850 hPa, which is also used to track synoptic systems. Polar lows have a smaller scale than synoptic lows, and also come with very strong surface wind, in addition they do not necessarily penetrate as high up in the atmosphere. Therefore 925 hPa vorticity field would be more appropriate to extract the polar low track. Tests with both vorticity fields have been done, and they

are also listed in Table 3.2. From Table 3.2 we see that there are no large differences by using vorticity at these two levels, e.g. Test 1 (VOR850) gives 11 tracks and Test 8 (VOR925) gives 8 tracks, and Test 5 (VOR850) gives 3 tracks and Test 11 (VOR925) also gives 3 tracks. However, the vorticity at 925hPa tend to pick up the tracks earlier in the forecast, and the tracks from vorticity at 850hPa tend to end later in the forecast (not shown). Overall, we decided to employ vorticity at 925 hPa.

Also, performing the tracking algorithm on the vorticity field gives the user the possibility to adjust a vorticity threshold, which needs to be exceeded of the detected positions. As seen from Table 3.2 the numbers of detected tracks are very sensitive to this threshold. At first in the codes of Hodges (1994, 1995, 1999) the detected vorticity features had to exceed a threshold value of $2 \times 10^{-5} s^{-1}$ (Test 1 and 8). By increasing the threshold, the number of detected tracks decreased (e.g. going from Test 1 to Test 4 reduced the number of tracks from 11 to 4). Aiming to extract the strongest track, for this particular case we became in the end confident to set the threshold to $1 \times 10^{-4} s^{-1}$.

Further objective criteria

After being content with the filtering interval of 200-600 km, zero minimum horizontal displacement, the minimum lifetime of 12 hours and vorticity threshold to be $1 \times 10^{-4} s^{-1}$, there were still too many tracks, and further objective criteria were needed. In the study of Zahn and Storch (2008) they introduced a third step after the filtering and tracking algorithm step; some additional constraints which were inspected along each individual detected track. The constraints used in Zahn and Storch (2008) include: A very strong filtered minimum (in the MSLP field), strong surface speed, static stability, a southward displacement and the track to be located over ocean (no land). These new objective criteria reduced the total number of tracks substantially. We wanted to adopt some of these, aiming to reduce the number of falsely detected tracks. The no land requirement in Zahn and Storch (2008) is a necessarily constraint to exclude false disturbances over land, and was employed in this experiment. Since polar lows comes with surface winds near or above gale force (Rassmussen and Turner, 2003) a new criteria would include the 10 m wind to exceed a given threshold. In addition, polar lows are often associated with cold air outbreak, and this yields high temperature differences between the sea surface and aloft. Noer and Ovhed (2003) at met.no uses the temperature difference between sea surface temperature (SST) and T500 (temperature at 500 hPa) as an indication for possible polar low developments. Therefore a further criterion would require the temperature difference between SST and T500 to exceed 43 K.

In Zahn and Storch (2008) the 10 m wind speed had to exceed 13.9 m/s at leas 20% of the positions, and the temperature difference should be above 43 K at lest once along the track. In the codes of Hodges (1994, 1995, 1999) a search of maximum 10 m wind speed and temperature difference within a radius around the detected tracks was done, then a percentage of the positions that fulfilled the constraints was calculated.

In contrasts to Zahn and Storch (2008), all of the detected tracks fulfilled these two

criteria at all the positions, so the number of tracks were not reduced. Originally, we searched for a maximum of the wind speed and temperature difference within a radius of 5° (500 km) around the detected positions. 5° search radius is too large, and this did not reduce any of the first detected tracks. In Zahn and Storch (2008) a radius of 100 km (approximately 1°) was used to look for wind maxima around the feature points, and this was adopted here. But still, very high surface wind speed and temperature difference were found within the 1° search radius, so the numbers of tracks were not further reduced. This indicates that the introduced criteria (i.e. vorticity threshold, lifetime, surface wind speed, vertically stability) do not necessarily extract the polar lows, and still there is need for other constraints.

Table 3.3: *The final constraints used in this study to track polar lows.*

		Constraints
Step 1	Filtering interval	200-600 km
Step 2	Minimum displacement	0
	Lifetime	12 h
	Vorticity threshold	$1 \times 10^{-4} s^{-1}$
Step 3	Objective criteria	
	(Within a search radius of 1°)	
	10 m wind speed	13.9 m/s
	SST-T500	43 K
	Other	No land

Ideally there should only be one or less track in every member. When performing the tracking algorithm on all the members from the UM-EPS-small and big with the constraints listed in Table 3.3, we still had too many detected tracks in every ensemble member (see Figure 3.3a). This problem was met by a subjective assessment, and the track with the strongest vorticity was extracted in every member (see Figure 3.3b). This was done by calculating the mean vorticity of every track from all the members. The track with the strongest mean vorticity in the control run was picked out (i.e. strongest track). Then the mean vorticity in every ensemble member was compared to the strongest track in the control run, and the track that exceeded the control mean vorticity the most times was chosen. In this way we were only left with the strongest track from every member.

We want to use the tracking algorithm to forecast the probability of an polar low track in addition to forecast the probability of the position of the polar low. At ECMWF a tracking algorithm is used to track tropical cyclones (TC) with all the members from the EPS (described in section 2.1), and a probability distribution of the area where the tropical cyclone most likely will pass is given in a strike probability map. The tracking algorithm used at ECMWF will not be discussed here. It should be mentioned that the tracking algorithm is only performed if there is at least one observation of the TC in a window of 6 hours around the analysis time (van der Grijn, 2002). This observation point of the TC and the steering flow is used to calculate the first guess of the next

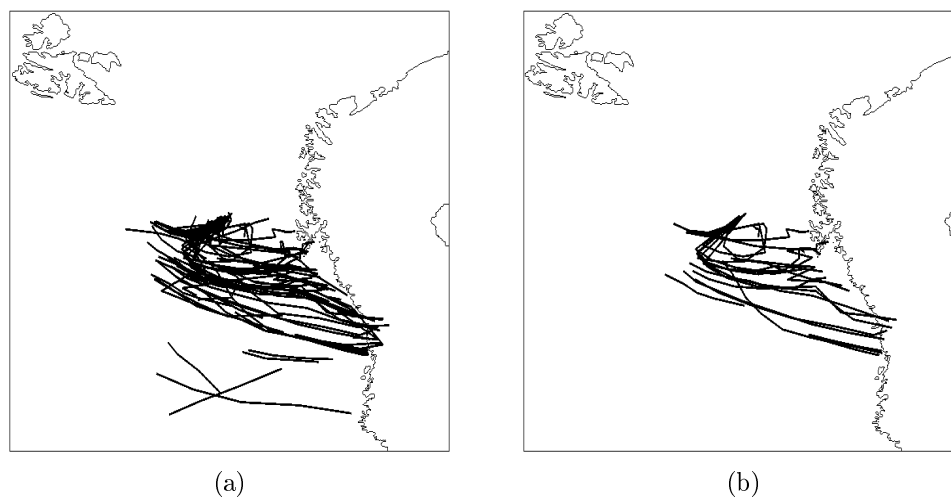(a)   (b)

Figure 3.3: *The track from UM-EPS-small. (a) shows all the tracks and in (b) the strongest track from every member is extracted.*

position. The TC is tracked for 120h, and statistics about the TC at every lead time is given. A strike probability map shows a horizontal map where the time dimension is eliminated and the track of every member (50 + 1) is plotted, regardless of what time the member predicted the TC. This is based on the fact that the forecaster is mostly interested in if there will be a TC and where it will go, rather than at what time the TC will occur. For instance, if all the members predict strong surface wind, but for a different lead time, this yields a low probability of strong wind over a long time frame. With the strike probability map this information diffusion is avoided.

A similar approach as described above would be desirable to apply to the polar low tracks. Figure 3.4 shows a Strike probability map analogous to what used at ECMWF. The strongest track in every member is extracted, same as seen in Figure 3.3b. Figure 3.4 shows the forecast probability that a polar low will pass within a square of 48km×48km during the next 60 hours. Even though there are many similarities between polar lows and tropical cyclones, the same method is not adequate for both. Polar lows tend to have a shorter lifetime than tropical cyclones, and they do not have the same propagation speed. As seen in Figure 3.4 an area get very high probability when the cyclone almost do not have any displacement. In addition, the tropical cyclone tracking algorithm is not performed without having at least one observation point, whereas here the tracking algorithm is performed on the forecast that started approximately 24 hours before the polar low was detected in the forecast.
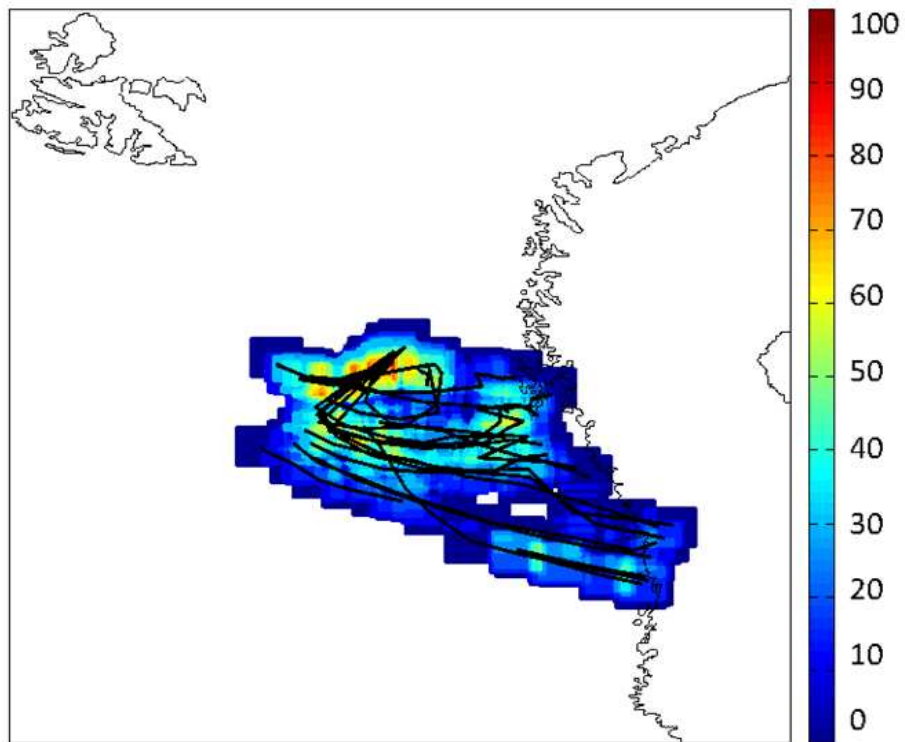
Figure 3.4: *Strike Probability Map from UM-EPS-small.*

Chapter 4

Results

In this chapter the results from the ensemble forecast UM-EPS-small and big will be presented. The forecast data will be compared both with observations and results from LAMEPS forecasts. First, the results for MSLP and pseudo satellite images are presented for each ensemble member.

The ensemble mean contains the most predictable parts in the flow, and is a supplement to the deterministic forecast. The spread between the members gives an indication of the predictability of the day. Therefore the ensemble mean and σ, with the purpose to investigate the spread between the members, thus the atmospheric predictability, are presented.

One purpose with ensemble prediction systems is to estimate the probabilities for different weather events during the forecast. This is simply done by calculating the fraction of members which catch the events, e.g. the forecast probability of strong wind or heavy precipitation. Hence, the forecast probability of wind speed, accumulated precipitation and potential temperature are compared with the campaign data.

In order to investigate the sensitivity of the results to model parameterization, additional sets of experiments were performed. For this purpose, the parameterization of the vertical mixing of the stable boundary layer was perturbed (see the boundary layer scheme described in Appendix A). In the end, the statistics from the tracking algorithm are shown.

We have mainly been focusing on comparing the forecasts with flight 3 (T + 42h) since the observations made at this time gives new information, and also at this time the polar low was well placed within the small domain. However, a few comparisons against flight 1 and 2 are also shown.

4.1   MSLP and pseudo satellite images

Figures 4.1 and 4.2 show the MSLP for lead time T+42h from UM-EPS-big and small, respectively, which is the secluded phase of the polar low. The satellite image in Figure

(a) HIRLAM20   (b) Member 00

(c) Member 01   (d) Member 02   (e) Member 03   (f) Member 04   (g) Member 05

(h) Member 06   (i) Member 07   (j) Member 08   (k) Member 09   (l) Member 10

(m) Member 11   (n) Member 12   (o) Member 13   (p) Member 14   (q) Member 15

(r) Member 16   (s) Member 17   (t) Member 18   (u) Member 19   (v) Member 20

Figure 4.1: *MSLP of HIRLAM20 analysis from 12 UTC 04.03.08 and UM-EPS-big at T+42h. The contour interval is 1 hPa. Member 00 is the control forecast.*

(a) HIRLAM20   (b) Member 00

(c) Member 01   (d) Member 02   (e) Member 03   (f) Member 04   (g) Member 05

(h) Member 06   (i) Member 07   (j) Member 08   (k) Member 09   (l) Member 10

(m) Member 11   (n) Member 12   (o) Member 13   (p) Member 14   (q) Member 15

(r) Member 16   (s) Member 17   (t) Member 18   (u) Member 19   (v) Member 20
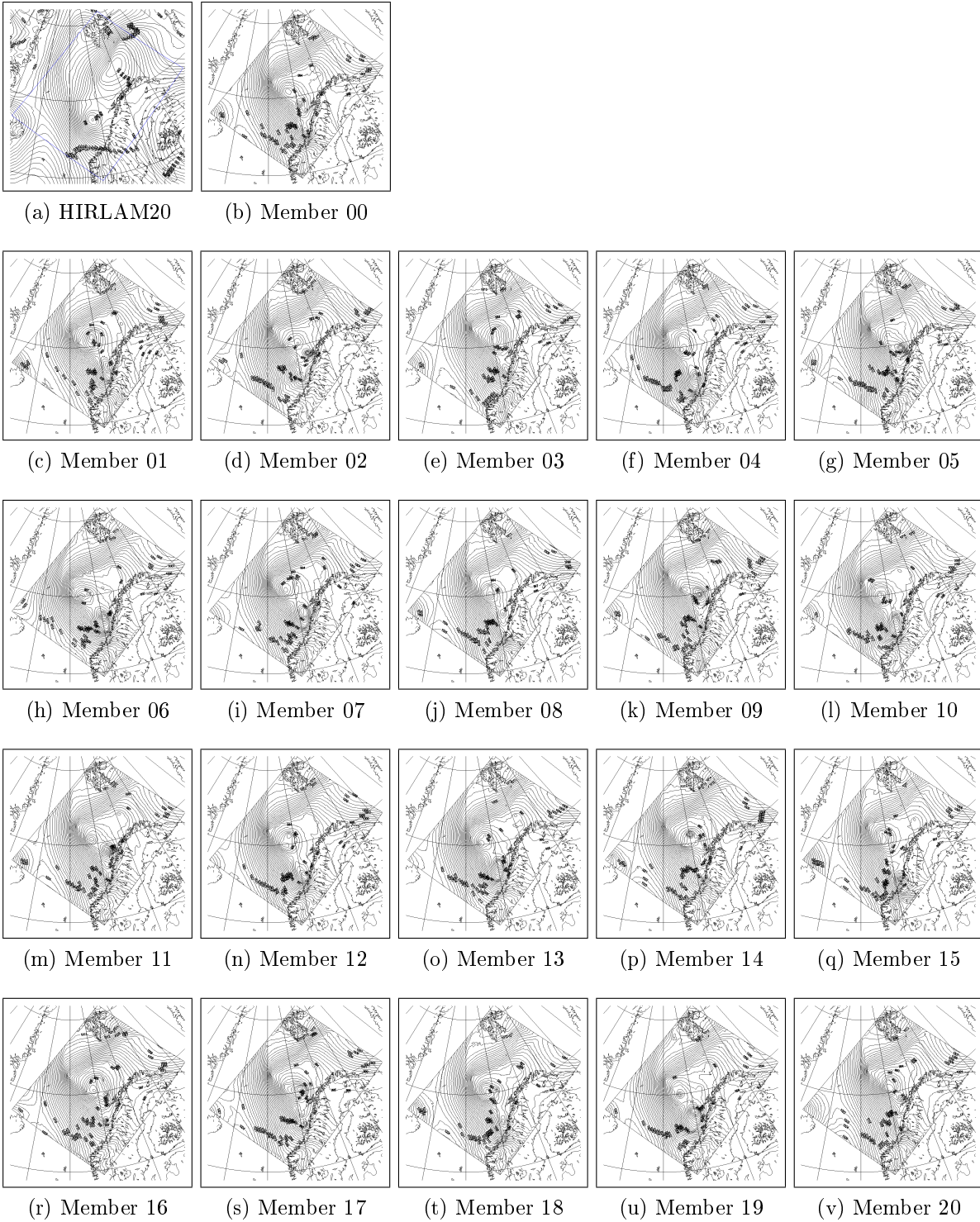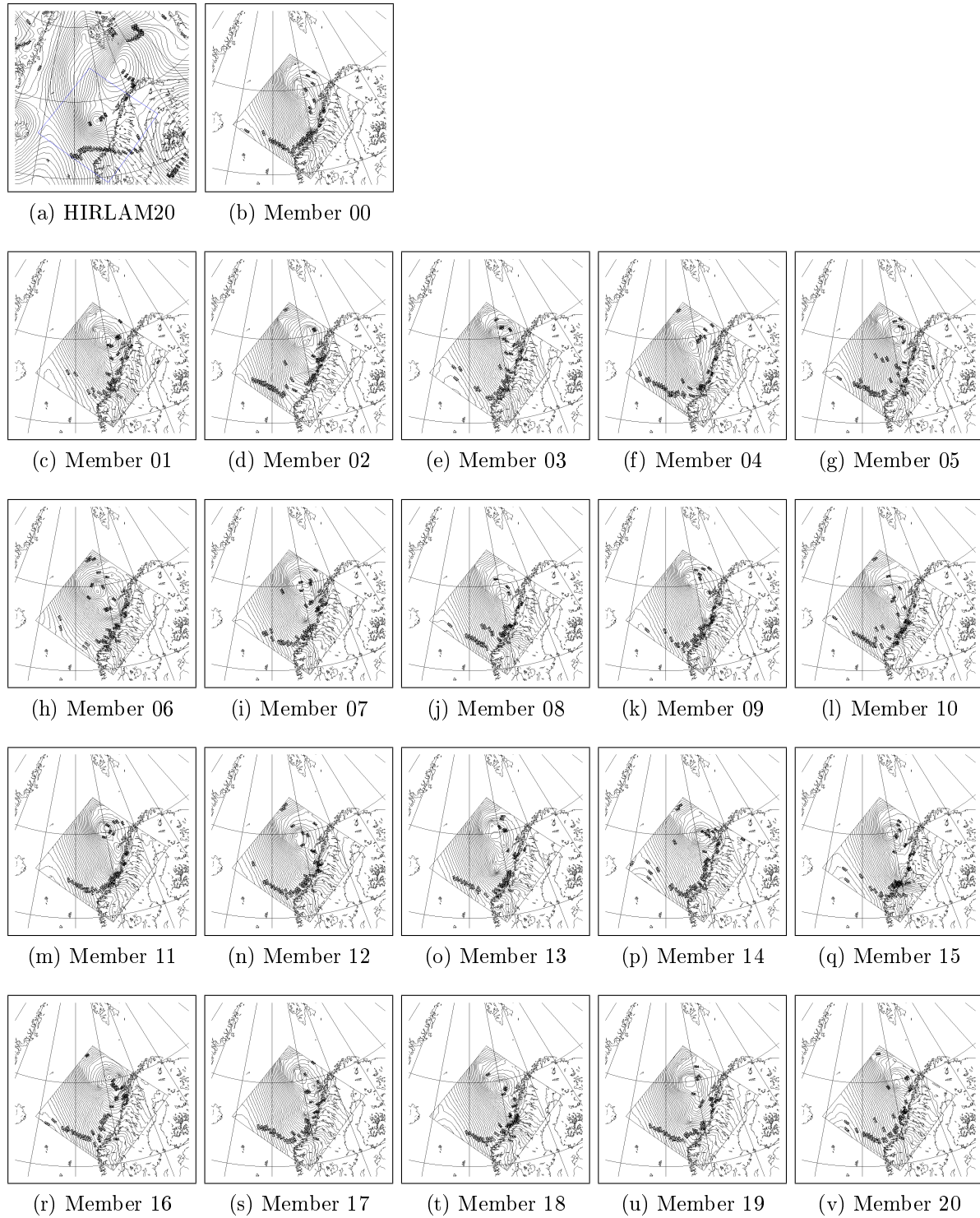
Figure 4.2: *MSLP of HIRLAM20 analysis from 12 UTC 04.03.08 and UM-EPS-small at T+42h. The contour interval is 1 hPa. Member 00 is the control forecast.*

(a) Satellite IR   (b) Member 00

(c) Member 01   (d) Member 02   (e) Member 03   (f) Member 04   (g) Member 05

(h) Member 06   (i) Member 07   (j) Member 08   (k) Member 09   (l) Member 10

(m) Member 11   (n) Member 12   (o) Member 13   (p) Member 14   (q) Member 15

(r) Member 16   (s) Member 17   (t) Member 18   (u) Member 19   (v) Member 20

Figure 4.3: *Satellite IR image valid at 11.37 UTC 04.03.08 and pseudo satellite images from UM-EPS-big at T+42h. Member 00 is the control forecast.*

(a) Satellite IR   (b) Member 00

(c) Member 01   (d) Member 02   (e) Member 03   (f) Member 04   (g) Member 05

(h) Member 06   (i) Member 07   (j) Member 08   (k) Member 09   (l) Member 10

(m) Member 11   (n) Member 12   (o) Member 13   (p) Member 14   (q) Member 15

(r) Member 16   (s) Member 17   (t) Member 18   (u) Member 19   (v) Member 20

Figure 4.4: *Satellite IR image valid at 11.37 UTC 04.03.08 and pseudo satellite images from UM-EPS-small at T+42h. Member 00 is the control forecast.*

2.4c and the analysis in Figure 2.5c are valid at the same time, but for convenience they are repeated here. The central pressure to the polar low from the HIRLAM20 analysis was 996 hPa. It can bee seen that for both domain every perturbed member have developed a different solution, and the spread between the members are largest for UM-EPS-big. For the big domain there can be seen several closed contours in every member. For instance, the control run has four closed contours, and the deepest low has central pressure of 986hPa. Several of the members have a large relative vorticity just off the Norwegian coast, close to Andøya. The control run of UM-EPS-small have two closed contours, where the deepest central pressure is 989 hPa. Many of the members in UM-EPS-small also have more than one closed isobar, and some of the cyclones are close to the Norwegian coast, but they are not as strong as those in UM-EPS-big. All the members in UM-EPS-big and small have one or more cyclones in the vicinity of where the polar low is observed in the satellite image and the analysis.

Figure 4.3 and 4.4 show the calculated cloud top temperatures from the two domains for the same lead time. The CTT images from the big domain all have high clouds north west of the Norwegian coast, which is in good agreement with the high clouds associated with the synoptic low. The differences between each image are largest in the area where the individual member have a cyclonic structure. The convective cells which are associated with the cold air outbreak are seen west of the observed polar low in the satellite image. Similar features can also be found in all of the members in the western part of the domain. For the small domain each member has signatures resembling spiral bands around a cyclone, and this is in the same area as the observed polar low. However, this is also the area where there are largest differences between each member, which is consistent with the results for the big domain. Furthermore, the CTT image from the small domain all have the convective cells west in the domain and high clouds in the top corner, consistent with the observations.

The transient evolution for each ensemble member of MSLP and CTT images from both systems are diverging with forecast lead time (not shown). This is as expected, since the perturbations will grow during the forecast. However, it is only after lead time T + 24 h that the systems are starting to diverge rapidly, which coincides with the early phase of the polar low.

4.2   Ensemble mean and spread

The ensemble mean and spread, as measured by the RMS deviation, σ, of LAMEPS, UM-EPS-small and big for T + 42h can be seen in Figure 4.5. The satellite image and the analysis from the same time are seen in Figure 2.4c and 2.5c. LAMEPS and UM-EPS-small have a closed contour at the same place, west of Andøya, but the lows have different central MSLP, LAMEPS has 991 hPa and UM-EPS-small has 989 hPa. UM-EPS-big has developed two cyclones where one is located close to Andøya, and the other one is further north-west. Both have a central MSLP of 988 hPa. σ for all the three systems increases with forecast lead time (not shown), and the spread is largest in the area close to where the polar low was observed (see Figs. 2.4c and 2.5c). For the

large domain, σ is also large close to the coastline where second low is situated. This is either a result of each member having different central pressure or that they are placed in different areas. From Figure 4.1 we see that a combination of these two is a fact.

The difference between the MSLP ensemble mean and σ of UM-EPS-small and LAMEPS, UM-EPS-big and LAMEPS and UM-EPS-big and UM-EPS-small are also seen in Figure 4.5. The differences between UM-EPS-small and LAMEPS (Fig. 4.5d) are small, and as a result of different central pressures the largest difference in ensemble mean is where both systems have a closed contour. The differences between UM-EPS-big and UM-EPS-small (Fig. 4.5b), and UM-EPS-big and LAMEPS (Fig. 4.5f) are on the same place. Where all the three systems have a low, there are differences in the MSLP ensemble mean due to different central pressures. In the area close to the coastline where only UM-EPS-big has a second cyclone and large spread, there are differences between UM-EPS-big and the two other systems in ensemble mean and σ.
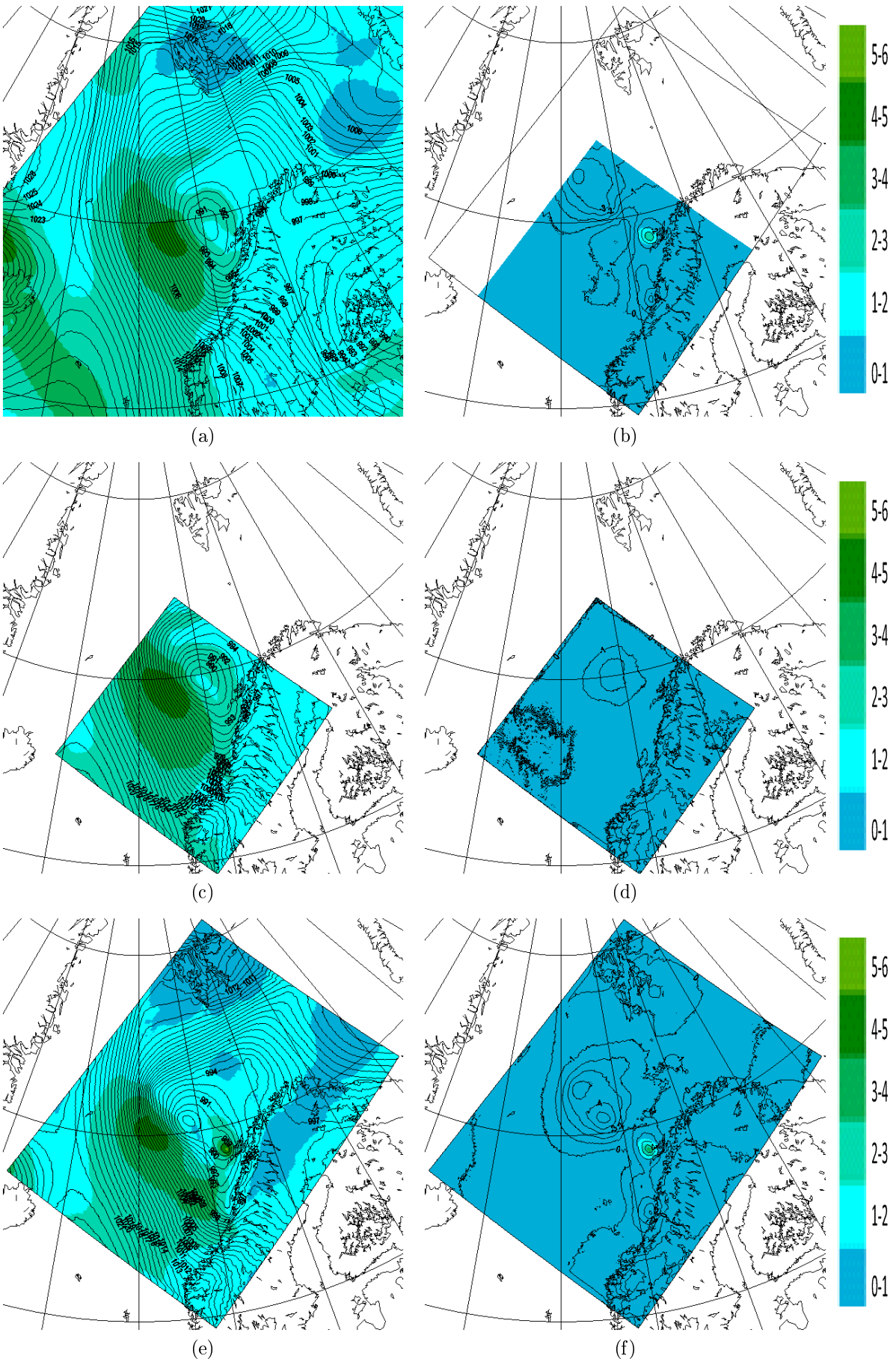
The ensemble mean in the three different systems capture the large scale flow to a good degree. However, in UM-EPS-small and LAMEPS there is only one cyclone which is placed between the observed synoptic low and the polar low. UM-EPS-big has two cyclones, where one is almost on the same place as for UM-EPS-small and LAMEPS, and the other one is closer to the coastline. The ensemble mean is expected to be just as skillfull as the control run in the early range of the forecast, and more skillful thereafter (Palmer et al., 2006). In addition, the ensemble mean filters out the unpredictable parts, and contains the most predictable part of the flow. This means that the most extreme weather events will not be seen in the ensemble mean. The ensemble means for the two systems (big and small) are smoother than their respective control runs. And for this long lead time it would not be expected to see a polar low in the ensemble mean, in line with its decreasing predictability. Thus there is a need to look for the probability of the extreme events.

4.3 Forecast probability compared with campaign data

Polar lows are associated with strong wind and heavy precipitation. Such extreme weather events are rare by nature. Therefore a probabilistic forecast is needed, to better reproduce the probability distribution of all the different weather events. By showing the probability of different meteorological parameters, the risk of occurrence of the extreme weather events will be forecasted. In the following we present the estimated probability of wind speed, accumulated precipitation and potential temperature exceeding different thresholds. The probability is estimated as the fraction of ensemble members exceeding the thresholds.

Forecast probability of wind speed

Figure 4.6 shows the forecast probability of wind speed > 20 m/s at 925 hPa at lead time T + 18h, T + 24h and T + 42h. These estimated probabilities are compared against the wind observations from flight 1, 2 and 3, respectively. The strongest wind
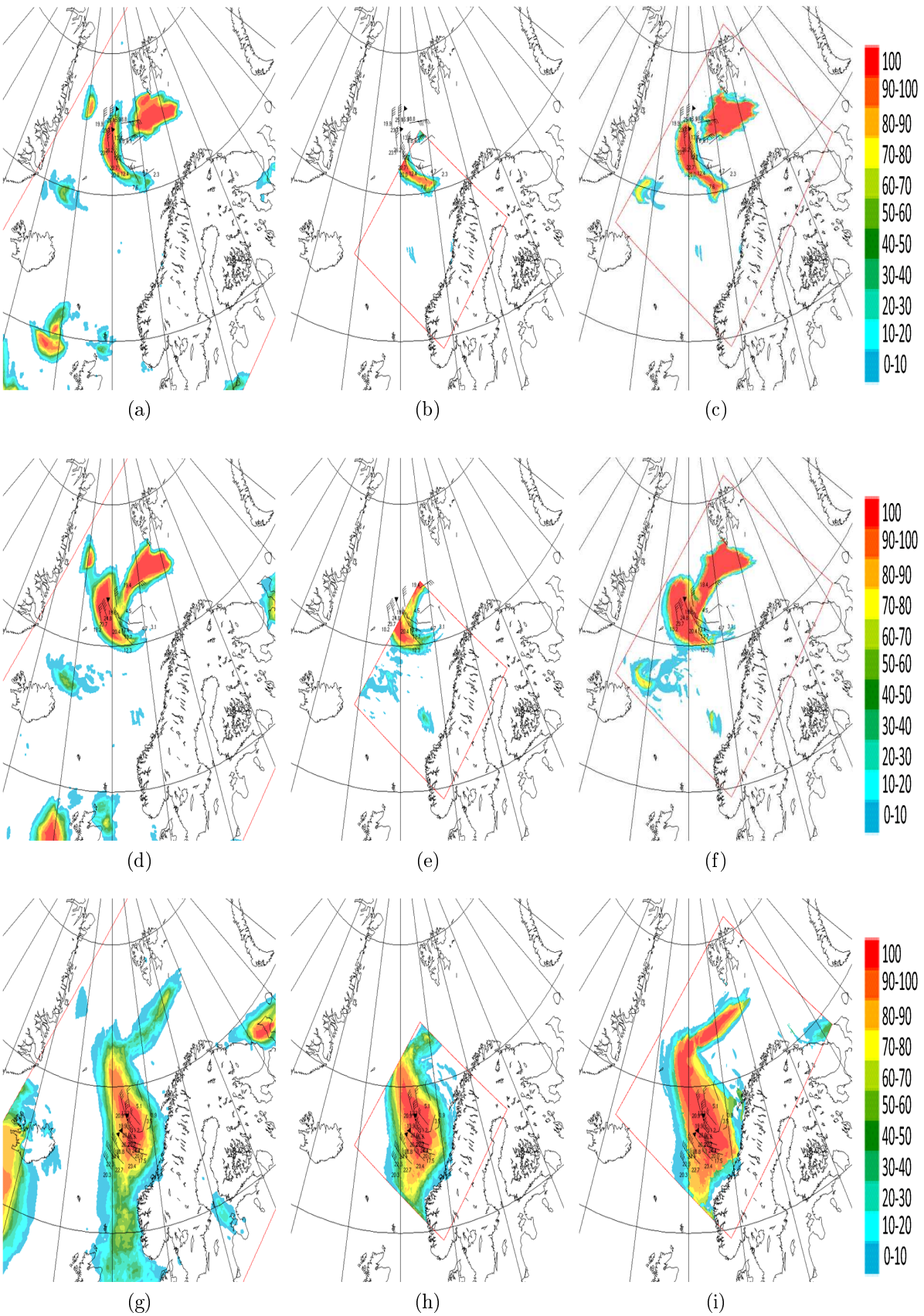
Figure 4.5: *MSLP ensemble mean and the spread at lead time T + 42h from LAMEPS
(a), UM-EPS-small (c) and UM-EPS-big (e). The black contours are the mean with 1
hPa contours. The shading is σ. The difference between ensemble mean and σ of UM-
EPS-big and UM-EPS-small (b), UM-EPS-small and LAMEPS (d), and UM-EPS-big
and LAMEPS (e).*

Figure 4.6: *Forecast probability of wind speed at 925 hPa > 20 m/s from LAMEPS (left panel), UM-EPS-small (middle panel) and UM-EPS-big (right panel) for the lead times: T + 18h(top row), T + 24h (middle row) and T + 42h (bottom row) compared with observation data from flight 1,2 and 3, respectively. A half barb on the wind arrows is denoted 2.5 m/s and a full barb is 5 m/s. A flag is 25 m/s wind speed.*

observed was 26.2 m/s (flight 1), 24.8 m/s (flight 2) and 28.0 m/s (flight 3). LAMEPS, UM-EPS-small and big all have 100% estimated probabilities in the area where the strongest wind speeds were observed for all the three flights. But UM-EPS-big has a higher estimated probability over a larger area. It can also be seen that there are small differences between LAMEPS and UM-EPS-small. The observation data only covers a small area, therefore to verify the results over a larger area the HIRLAM20 (Figure 2.5c) analysis and QuikSCAT (not shown) are used. From the analysis and QuikSCAT observations it is seen that the upper tails with high probability found in LAMEPS and UM-EPS-big (the small domain does not cover the area) for all the three lead times, are consistent with the strong wind speed associated with the synoptic low.

Wind up to 28 m/s was observed during flight 3, therefore the estimated probability of wind > 25 m/s is shown in Figure 4.7. For this threshold, UM-EPS-big has a higher probability (up to 100%) over a much larger area than UM-EPS-small and LAMEPS. The small domain has a very small region in the center of the domain where all the members exceeded the threshold at the same place, but this cannot be seen for LAMEPS. However, the spatial distribution of where there is an estimated probability > 0 is the same for UM-EPS-small and LAMEPS. Further, the area where the probability of strong wind is located in the respective ensemble systems, is where the weak wind is observed. Thus, all the three ensemble systems have shifted the area of strong wind further north compared to the observations. Since the forecast probability is for lead time T+42h and the flights lasted over several hours, we wanted to see in what direction the area of strong wind was moving, and then maybe the location of the strong wind would coincide better with the observations at a different lead time. But the forecast probability of wind 6 hours before and after T + 42h showed that the strong wind propagated from northwest towards the coastline. Additionally, if we compare σ (Fig. 4.5), it can be seen that the high σ is on the same place as where the strong wind is predicted for all the three systems.

From the drop sondes released during the flights vertical cross sections have also been calculated. In this experiment we have chosen one cross section which crossed the low in its secluded phase and was well placed within the small domain. The cross section N-S is from flight 3 (T + 42h) and its geographic location is seen Figure 2.5c. Note that the observed wind speed (Fig. 4.8a) is interpolated from the drop sonde observations, where the black dots indicates where they were released. The probability of wind speed > 25 m/s from UM-EPS-small and big from the cross section at lead time T+42h is seen in Figure 4.8b and c, respectively. The low level jet can clearly be seen, where wind speed up to 30 m/s is observed. The high wind speed in the top right corner is the upper level jet stream. UM-EPS-small and big both predicted the low level jet, but it is shifted a bit northward. This is consistent with the horizontal forecasts probability of wind, where we saw the probability of strong wind to be located a bit further northeast than the observed strongest winds. The only significant difference between the two domains is that UM-EPS-big has a higher probability than the small domain.
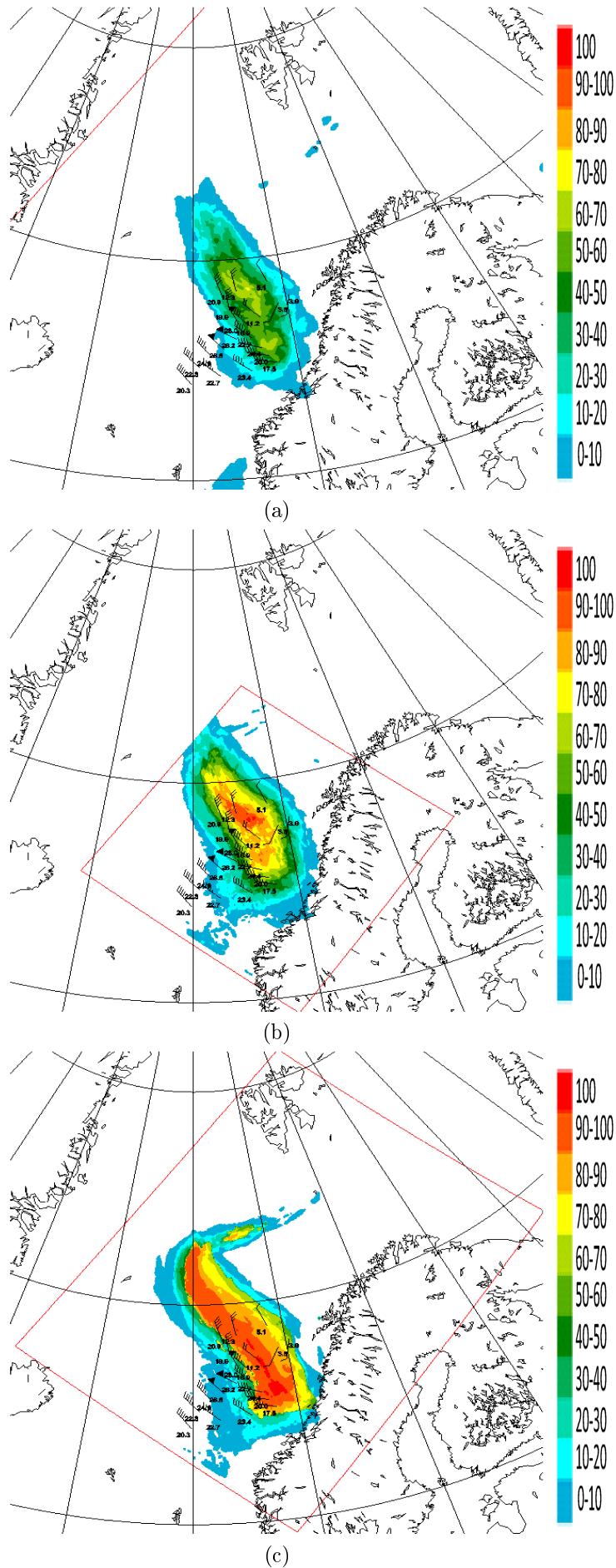
Figure 4.7: *Forecast probability of wind speed at 925 hPa > 25 m/s from LAMEPS (a), UM-EPS-small (b) and UM-EPS-big (c) at lead time T+42h compared with observation data from flight 3.*
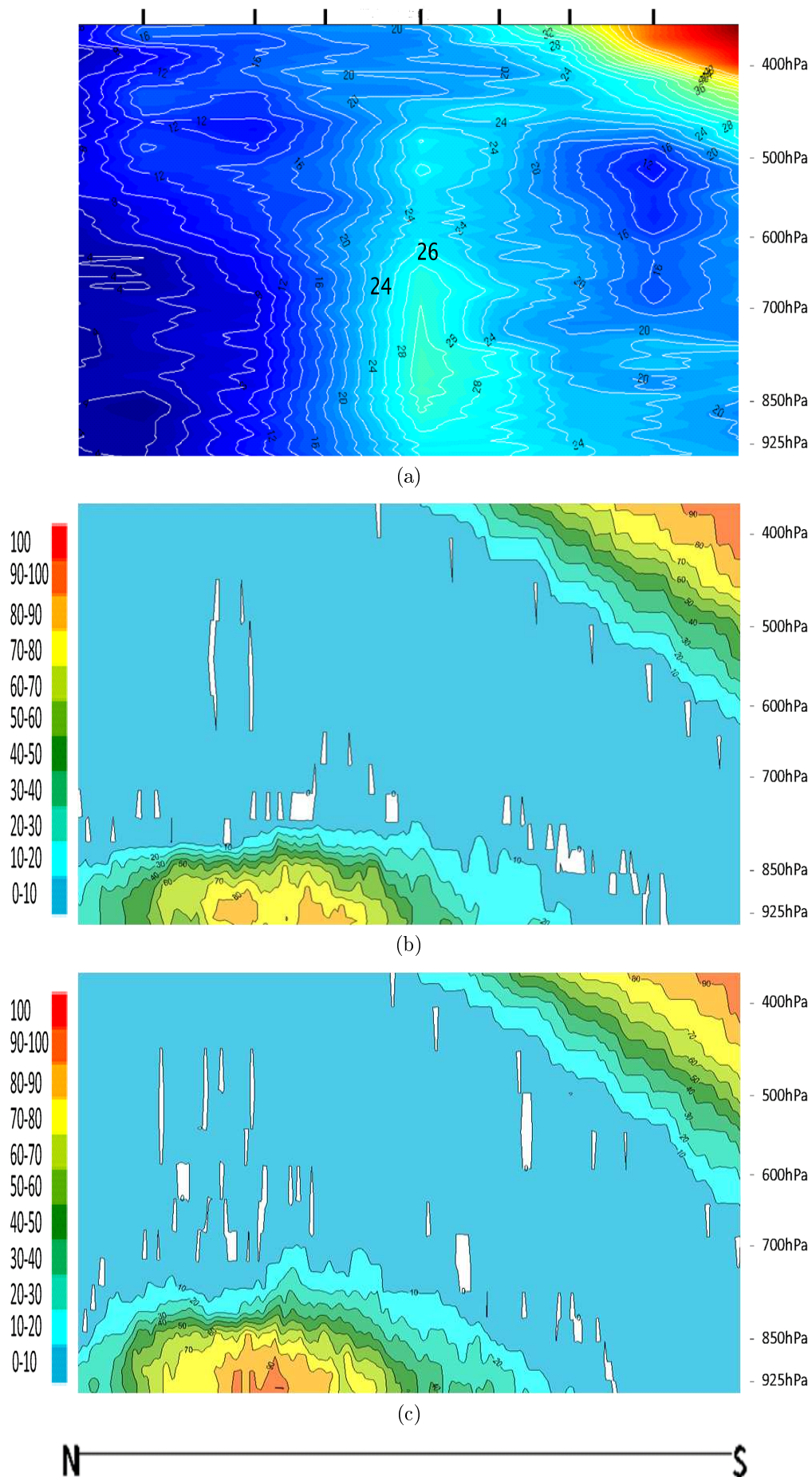
(a)

(b)

(c)

Figure 4.8: *Observed wind speed from flight 3 (a) and probability of wind speed > 25m/s at lead time T + 42h from UM-EPS-small (b) and UM-EPS-big (c). The contour interval in (a) is 2 m/s.*
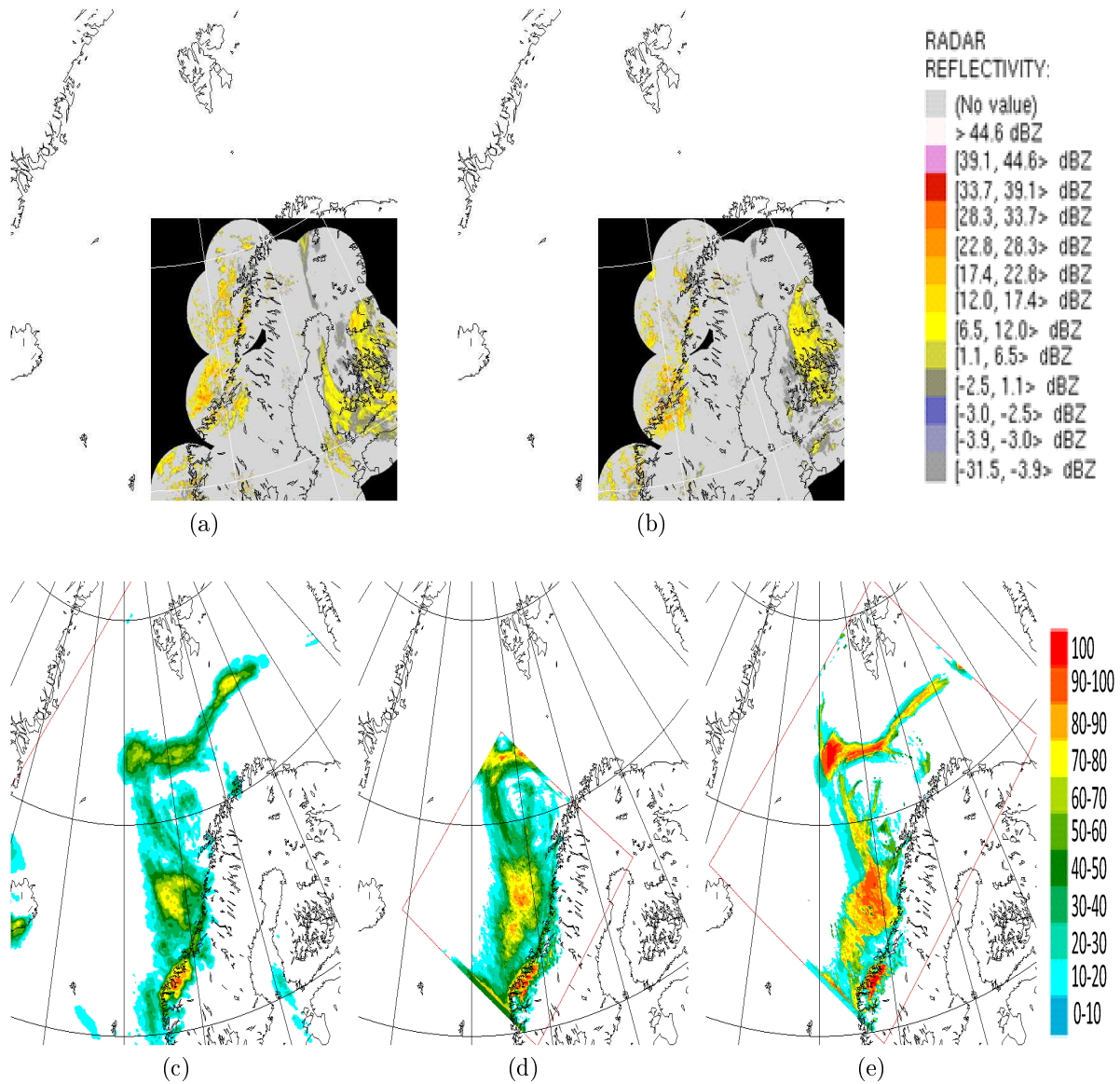
Figure 4.9: *Radar reflectivity from 06 UTC (a) and 12 UTC (b) 04.03.08 compared with forecast probability of accumulated precipitation > 2.5 mm/6h from LAMEPS (c), UM-EPS-small (d) and UM-EPS-big (e) for lead time T + 42h.*

Forecast probability of accumulated precipitation

The radar reflectivity for 06 UTC and 12 UTC 04.03.08 can be seen in Figure 4.9. Unfortunately at the time of the campaign, the radar at Andøya was in its initial stage, therefore the radar reflectivity was not converted to accumulated precipitation. Hence, the reflectivity instead of accumulated precipitation, is compared with the forecast probability. It is not clear whether the observed precipitation seen in Figure 4.9a and b is associated with the polar low or is a result of other weather phenomena. But anyhow, we want to see the effect of the downscaling, and then especially if the skill in forecasting

precipitation is being improved. Obviously, we can only verify the precipitation forecasts within observation radius of the radars, i.e. the coast region. From Andøya and down to Trøndelag there is high reflectivity at 06 UTC (Fig. 4.9a), which means there is a significant amount of precipitation. At 12 UTC (Fig. 4.9b) there is some precipitation outside Troms, but most precipitation is seen further south, off the coast in Trøndelag.

Figure 4.9 also shows the forecast probability of accumulated precipitation > 2.5 mm/6h from LAMEPS (c), UM-EPS-small (d) and big (e) for the lead time T + 42h. All the three systems have estimated probability > 0 in a large area outside the Norwegian coast. UM-EPS-big has 100% over a large region, mainly in the same place as the strong wind is predicted (Fig. 4.7), and also consistent with observed precipitation (outside Smøla). The small domain has 100% only over a very small area, but the area of lower estimated probability covers a large region. For LAMEPS there is 100% probability over land in the Møre and Romsdal county, and a few grid points outside the coast of Nordland. Generally, LAMEPS has lower probability of accumulated precipitation > 2.5mm/6h over a smaller area than UM-EPS-small and big, but for all the systems the probability is located on the same place. All the systems have some estimated probability outside Andøya, but UM-EPS-big has the highest probability, up to 50%.

Forecast probability of potential temperature

As a result of the flight campaign, observations of several meteorological parameters were obtained. Next, we compare the forecast probability of potential temperature with the same cross section as for wind speed. Figure 4.10a shows the vertical cross section of observed potential temperature from flight 3. The warm core of the polar low is evident, where the contours are dipping down to the ground. Also as described in section 2.3 we see that the cold air is found to the south and north of the core. There were not any differences between UM-EPS-small and big, therefore only the results from UM-EPS-big are shown. Figure 4.10b and c shows the forecast probability of potential temperature > 280 K and 270 K, respectively. Going from south to north the 280 K contour in the observation cross section starts at around 550 hPa and drops down to about 600 hPa and end at 500 hPa. There is some spread between the ensemble members around southern boundary of the cross section where we find the 280 K contour, Figure 5.10b, but above about 550 hPa the estimated probability is 100%. The area of probability is dipping down, as for the 280 K contour, but it does not go back up again. This indicates that UM manages to reproduce the cold air to the south, but it is too warm to the north. Furthermore, to see if the model captured the very cold air south of the core, the probability of potential temperature > 270 K is shown in Fig. 4.10c (The observed 270 K contour is found in the southern corner in Fig. 4.10a). There is some spread between the ensemble members where the 270 K contour starts. Also, some of the members do not capture the very cold air to the south, since there are estimated probability > 0 of potential temperature >270 K.
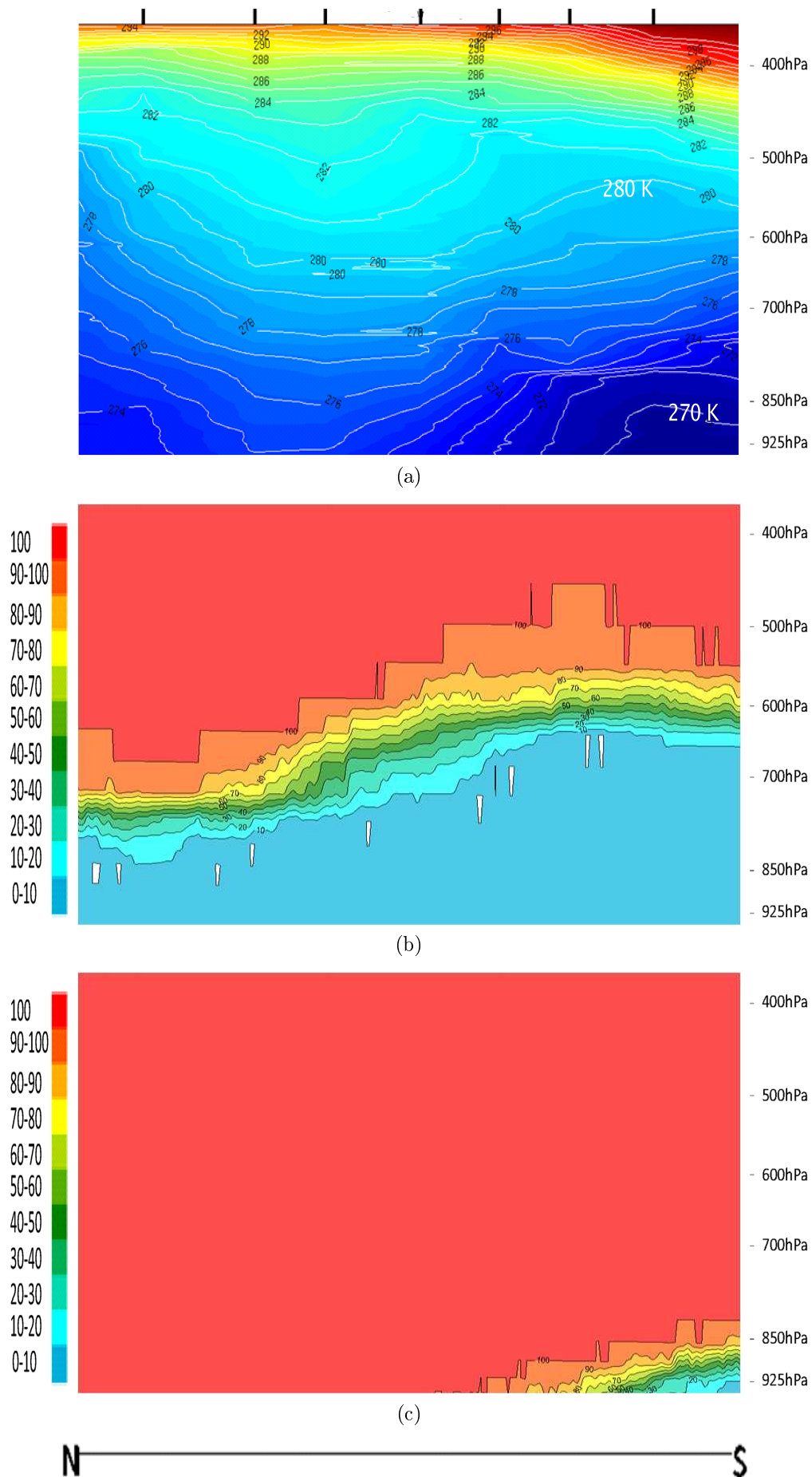
Figure 4.10: *Cross section of observed potential temperature from flight 3 (a) and probability of potential temperature > 280 K (b) and > 270 K (c) from UM-EPS-big at lead time $T + 42h$. The contour interval in (a) is 1 K.*
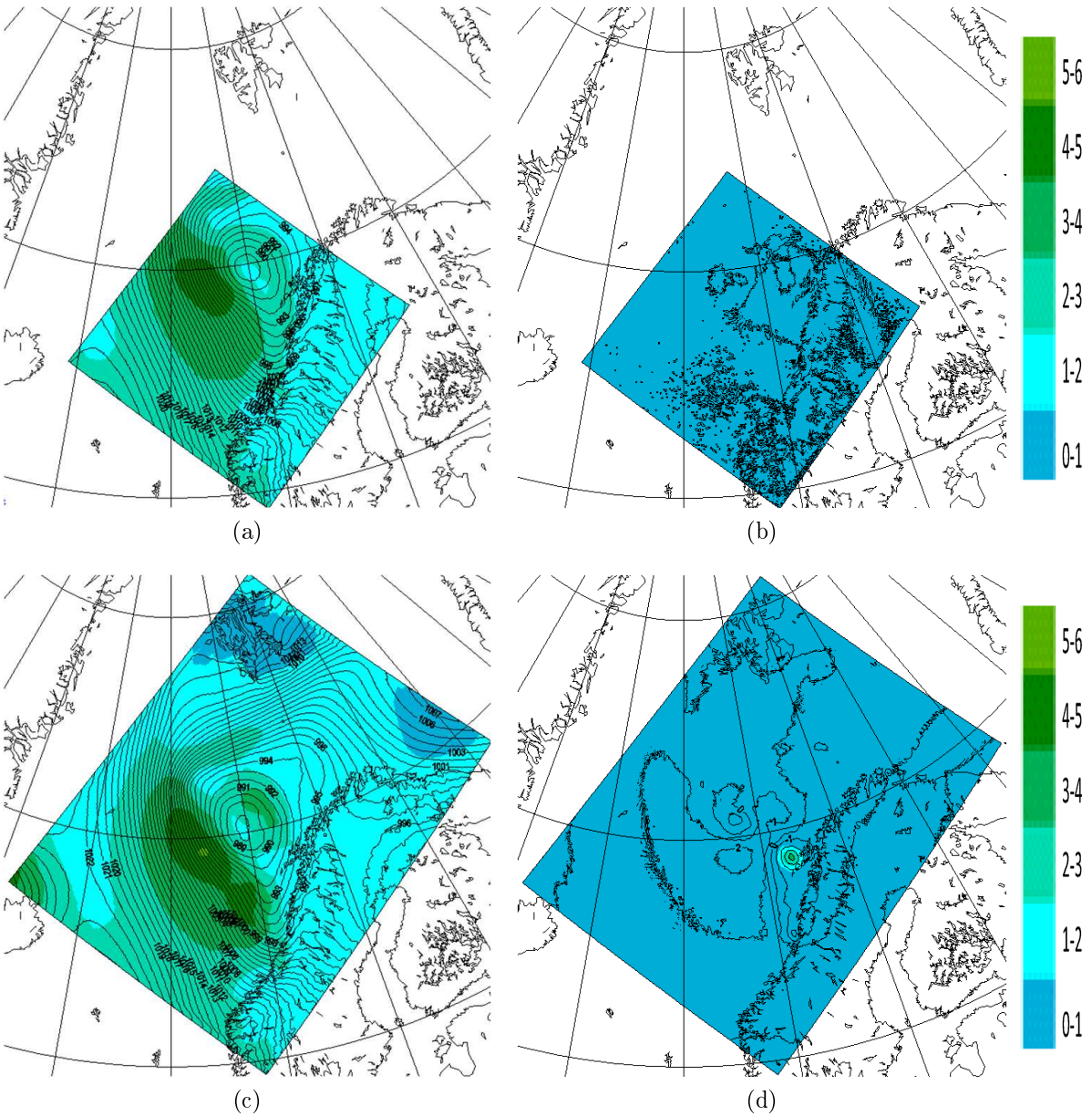
Figure 4.11: *MSLP ensemble mean and the spread of UM-EPS-small-lessvertical (a) and UM-EPS-big-lessvertical (c) at lead time T + 42h. The black contours are the ensemble mean with 1 hPa contours and the shading is the σ The difference of MSLP ensemble mean and σ between UM-EPS-small and UM-EPS-small-lessvertical (b) and UM-EPS-big and UM-EPS-big-lessverical (d).*

4.4   Perturbing the physics in the stable boundary layer

The operational configuration of UM at met.no includes a stability function which allows for an enhanced vertical mixing in the stable boundary layer. This is due to the complex orography over Norway, where the unresolved scales force more vertical mixing.
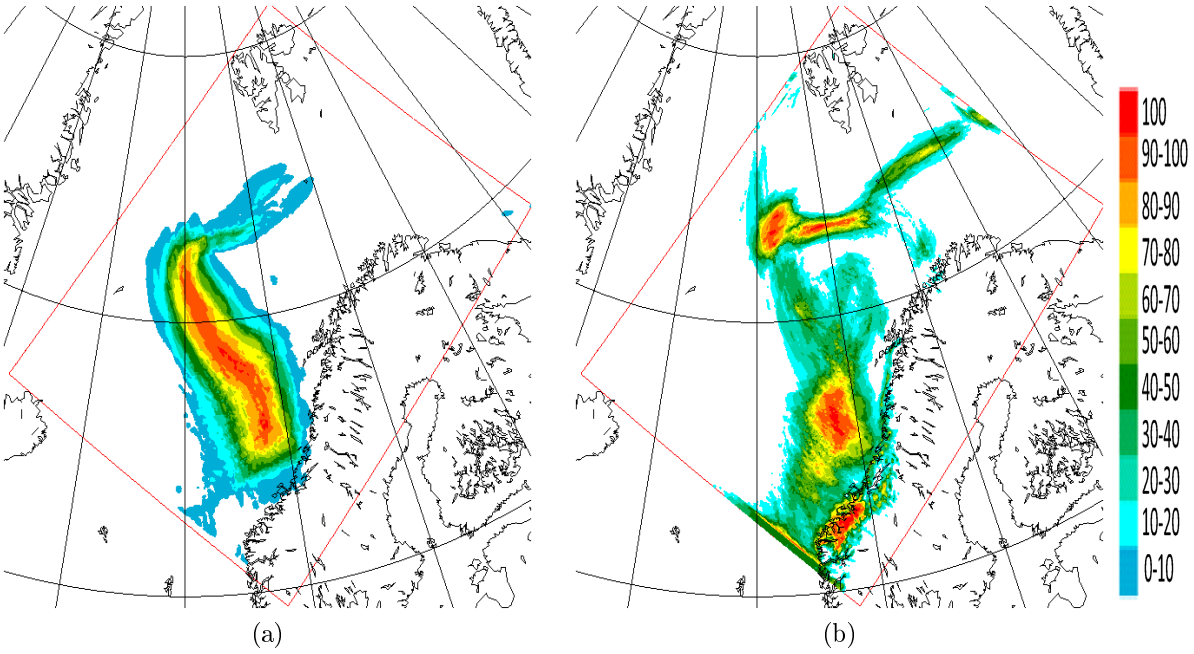
Figure 4.12: *Forecast probabilities for Um-EPS-big-lessvertical, where (a) shows probability of wind speed > 25 m/s and (b) the probability of accumulated precipitation >2.5 mm/6h.*

In Appendix A the boundary layer turbulence scheme is described. The two domains set up for this study are mainly over ocean, and therefore additional experiments with UM-EPS-small and big have been performed with a stability function that yields less vertical mixing in the stable boundary layer (see Appendix A). These two new experiments will be referred to as UM-EPS-small-lessvertical and UM-EPS-big-lessvertical, respectively. It needs to be emphasized that the perturbation only affects the physics of the stable boundary layer.

Perturbing the physics in UM-EPS-small had no effect on the results. Figure 4.11a shows the ensemble mean and σ of MSLP for UM-EPS-small-lessvertical, and Figure 4.11b shows the difference between MSLP ensemble mean and σ of UM-EPS-small and UM-EPS-small-lessvertical. From Figure 4.11b we see that there are not any large differences between the two runs. This is also consistent for the different forecast probabilities (not shown).

On the other hand, for UM-EPS-big the vertical mixing had an impact on the forecasts. The ensemble mean and σ of MSLP from UM-EPS-big-lessvertical are seen in Figure 4.11c, and Figure 4.11d shows the difference between UM-EPS-big and UM-EPS-big-lessvertical. In Figure 4.11c we see that in the experiment with less vertical mixing, there is only one cyclone with a central pressure of 988 hPa which is a bit further south than the cyclone in the original run. The differences between the two experiments are largest close to the coastline where the second cyclone and the high σ was located in

the original run. However, the high σ close to where the polar low is observed is found in both experiments. For the forecast probabilities there were some differences between UM-EPS-big and big-lessvertical. The original run has larger area of high probability than the perturbed run, and this is consistent for all of the different parameters. Figure 4.12 shows the forecast probability of wind speed > 25 m/s (Fig. 4.12a) and accumulated precipitation > 2.5 mm/6h (Fig 4.12b) from UM-EPS-big-lessvertical, compared with the original run, Figures 4.7c and 4.9e, respectively, it can clearly be seen that the area of probability is in the same place, but the region of high probability is larger for the original run than the perturbed run.

4.5   Tracking Polar lows

In this study the tracking algorithm of Hodges (1994, 1995, 1998) has also been explored. Its implementation and modification in order to track polar lows was described in section 3.2.2. Figure 4.13 shows all the tracks from every member (left panels) and the strongest track from each member (right panels) from the four experiments presented in this study. First looking at the left panels, we see that the runs done with the small domain have fewer tracks than the runs from the big domain and also that they cover a smaller geographical area. The former is consistent with the MSLP post stamp images, where we saw that UM-EPS-big tend to have more closed contours than UM-EPS-small. The latter is just a result of a smaller domain. However, the tracks from the two different ensemble systems are mainly placed in the same area. Moreover, there are no significant differences in the location of the tracks between the perturbed physics runs and unperturbed runs.

The location of the tracks between the two systems changes when only the strongest track is selected. First looking at UM-EPS-big and big-lessvertical, we see that the former have more tracks closer to the coastline outside Andøya than the latter. In addition, it is more spread between the tracks in the original run compared to the perturbed run. For UM-EPS-small and small-lessvertical there is also a change in the location of the tracks. There are more tracks further west in the domain for UM-EPS-small than found in the perturbed run. This is in contradiction to the results from MSLP ensemble mean, σ and different forecast probabilities where there were no significant differences between the two experiments. Comparing the tracks with the observations, Figs. 2.4 and 2.5, the location of the strongest tracks for all the systems are close to the area where the observed polar low propagated.

In addition, section 3.2 presented a method to forecast the probability of polar lows and their tracks analogous to the strike probability map at ECMWF. The results can be seen in Figure 4.14. From Figure 4.14 it can clearly be seen that each system has the strongest tracks in different positions. UM-EPS-big has a higher probability of a polar low close to the coast outside Andøya, and the same is seen for UM-EPS-small lessvertical. UM-EPS-small have more tracks further west in the domain. Comparing all the four runs, it seems as though UM-EPS-big-lessvertical has the smallest spread between the members.
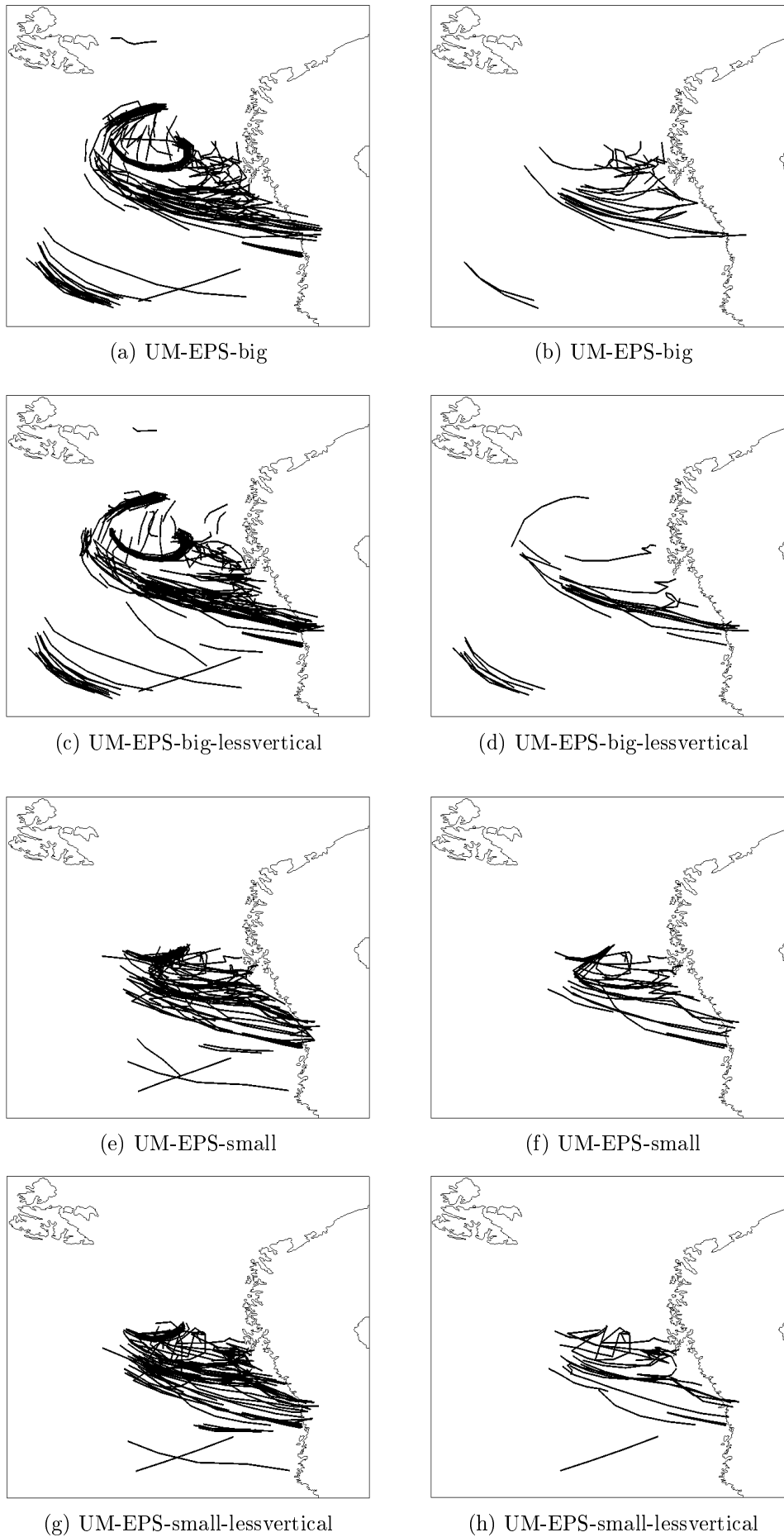
(a) UM-EPS-big

(b) UM-EPS-big

(c) UM-EPS-big-lessvertical

(d) UM-EPS-big-lessvertical

(e) UM-EPS-small

(f) UM-EPS-small

(g) UM-EPS-small-lessvertical

(h) UM-EPS-small-lessvertical

Figure 4.13: *Results from the tracking algorithm. Left panel shows all the tracks from all the members from all the four runs done, and in right panel the strongest track in every member is extracted.*
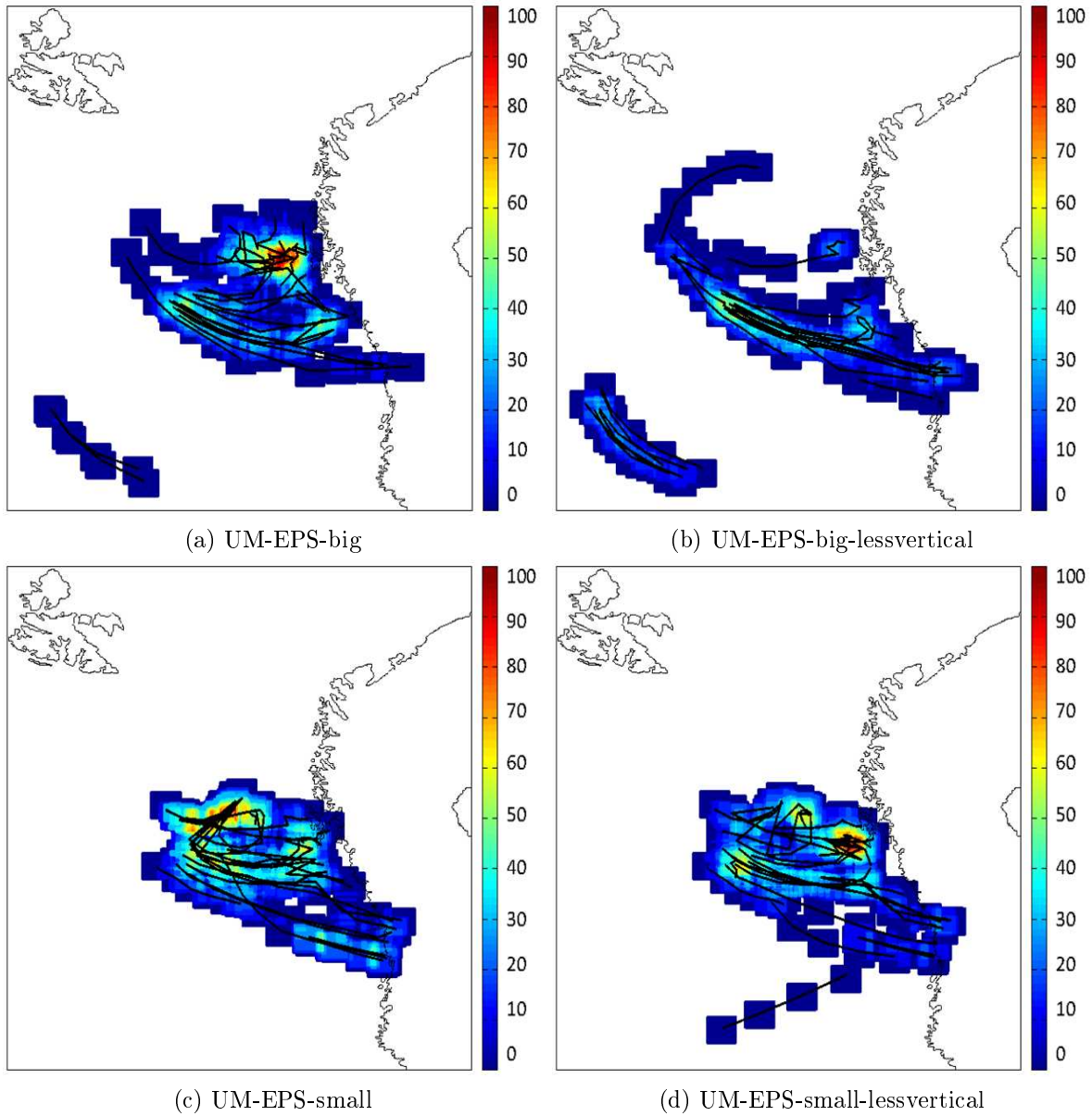
(a) UM-EPS-big

(b) UM-EPS-big-lessvertical

(c) UM-EPS-small

(d) UM-EPS-small-lessvertical

Figure 4.14: *Forecast probability of polar lows and the position within a square of 48 km × 48 km during the next 60 hours.*

Chapter 5

Summary and Discussions

In this experiment LAMEPS has been downscaled with the non-hydrostatic model UM, and two new domains have been set up with the purpose to see how the integration size affect the prediction. LAMEPS is run with the quasi-hydrostatic model HIRLAM where it employs 12 km grid spacing and 60 levels. The two UM domains both have a horizontal grid mesh of 4 km and 38 levels. The predictability of extreme weather have been investigated related to a polar low event that was extensively observed during the IPY-THORPEX campaign (IPY-THORPEX, 2009). Regular observation data and observation data from the campaign have been compared with the ensemble mean and the spread between the members in addition to the probability of different parameters. Further, two new methods to analyze the model outputs have been carried out: Pseudo satellite images and a tracking algorithm to track polar lows path. The following is a summary of the main findings:

- The MSLP of UM-EPS-small and big diverge with lead time. Stamps images show, to a great extent, large spread between each member for both systems at lead time T + 42h, but the spread is larger for UM-EPS-big. There are several vortices in every member for both systems, however, the members in UM-EPS-big tend to have more closed contours than UM-EPS-small.

- The pseudo satellite images show for both systems convective clouds west in the domains as a result of the cold air outbreak. However, for both systems there is largest spread between each member in the area where there is a cyclonic structure.

- The differences between the members in UM-EPS-small and big for MSLP and pseudo satellite images are largest in the area of the observed polar low.

- In the early range of the forecast the ensemble mean and the control run for UM-EPS-small and big have a similar solution, and thus with increasing lead time they gradually diverge. At lead time T+42h, the ensemble mean from UM-EPS-small looks very similar to LAMEPS, whereas UM-EPS-big looks more dissimilar. UM-EPS-big has developed two cyclones, compared to only one in UM-EPS-small and LAMEPS. σ also increases with lead time for the three systems, and at T+42h it is largest in the area of the observed polar low and also where the strong wind is predicted.

- The estimated forecast probability of wind for LAMEPS, UM-EPS-small and big have high probability of strong wind for the lead times T + 18h, T + 24h and T + 42h, consistent with the observed wind from the flights. However, UM-EPS-big has a larger area of high probability than LAMEPS and UM-EPS-small. Wind up to 28 m/s was observed for lead time T+42h, and for the threshold wind speed >25 m/s, LAMEPS had no area where all of the members predicted wind with this strength, UM-EPS-small had only a small region and UM-EPS-big had the largest region with high estimated probability. The vertical cross section of probability of wind also shows that more members in UM-EPS-big than UM-EPS-small predicts stronger wind.

- The estimated forecast probability of accumulated precipitation shows there is a great advantage increasing the horizontal grid resolution in addition to using a non-hydrostatic model. The three systems (LAMEPS, UM-EPS-small and big) have the region of estimated probability > 0 at the same place, but LAMEPS has the lowest estimated probability and UM-EPS-big has highest estimated probability. The only place to verify the model results against observations is along the Norwegian coast. In the area where there is observed precipitation, an estimated probability > 0 of precipitation is forecasted for all three systems, and UM-EPS-big has the highest estimated probability.

- There were small differences between UM-EPS-small and big for estimated probability of potential temperature. The potential temperature probability shows that UM tends to have some difficulty in reproducing the warm and cold advection at the surface. At lead time T+42h, the model reproduces the cold air to the south that has been advected from the north. However, some of the members tend to have difficulties in producing the very cold air (270K). Also, the cold air that has been advected all the way to the north of the core is not seen in the model results. In this region, the model is warmer than observed.

- When looking at the ensemble mean and forecast probabilities, perturbing the physics in the stable boundary layer only led to differences in UM-EPS-big, where the second cyclone found in the ensemble mean of the original run was removed from the perturbed run. Also, the area of high probability of strong wind and heavy precipitation was reduced for UM-EPS-big-lessvertical compared to the original run.

- The tracking algorithm showed that UM-EPS-small and big (perturbed and unperturbed) located the different ensemble tracks mainly in the same region. However, when extracting the strongest track, there was a change in the location of the tracks for the four different experiments. This means that the strength and location of the vorticities is very sensitive to the domain size and the physical parameterization.

The new information added by UM-EPS-big is highly improved, especially for a longer lead time. The differences between UM-EPS-big and LAMEPS are smaller in the early range of the forecast and for a lower probability threshold (see Fig. 4.6) than for lead

time T+42h, where there is a higher probability of extreme weather (e.g. strong wind; Fig. 4.7 and heavy precipitation; Fig. 4.9). The small domain seems to be too small and therefore is more restricted by LAMEPS than the big domain. However, there is some improved predictability for UM-EPS-small compared to LAMEPS for longer lead time, but the amount of new information added is not as enhanced as for UM-EPS-big. The improvements in the forecast seen in Fig. 4.7 and 4.9 for UM-EPS-small and big are evident, but with limitations of solutions associated with a smaller domain.

In addition to the sensitivity of the domain size, the results show that the physical parameterization also affects the forecast. The perturbation of the SBL had the largest effect on the big domain, where the decrease in vertical mixing in the SBL reduced the area of high probability for strong wind and precipitation and removed the second cyclone in the original run. Interesting results were also found when the tracking algorithm was performed on the outputs from the different runs. The perturbation affected the location of the strongest tracks in every member. There were more tracks closer to the coastline and a larger spread between the tracks in the original set up than the perturbed run for the big domain. The warm air section is found close to the coastline in the early range of the forecast. When the atmosphere is warmer than the ground (here the ocean), the air becomes more stable, and this is why the effect of perturbing the SBL parameterization is largest in this region, when compared to where there is a cold air outbreak and more unstable air masses.

For the small domain there was also a change in the locations of the strongest tracks between the perturbed and unperturbed experiments, which is particularly interesting since there were no large differences in the ensemble mean and forecast probabilities. This emphasizes the fact that when downscaling, the domain is very sensitive to the size and location as well as the physical representation. The sensitivity of the strength of the vorticity is clearly seen in Figure 4.14, which shows the forecast probability of a polar low and the positions within a square of $48km \times 48km$ during the next 60 hours. All four experiments have the strongest tracks in a different region. Note that there are some dissimilarities between Figure 4.14 and the strike probability map at ECMWF. For instance, if a polar low does not propagate far enough within the next time frame, there will be high probability in that area.

UM-EPS shows improvements in producing precipitation compared to LAMEPS (see Fig. 4.9) However, 4 km horizontal grid spacing is still too coarse to adequately represent deep convection. UM run with 4 km resolution has the convection partly parameterized and partly calculated explicitly (see the convection scheme described in Appendix A). This is done on the basis that the convection cannot be explicitly resolved at 4 km since the convective updraft may occur on a smaller scale, and the assumption for the parameterization is not valid with 4 km grid spacing (Deng and Stauffer, 2006). This yields convective rainfall difficult to predict in 4 km models. Previous studies performed with UM shows that a 4 km model do not have the same level of performance in predicting precipitation as a 1 km model, where the convection is only calculated explicitly (Roberts and Lean, 2007; Lean et al., 2008).

The results presented here are consistent with Xue et al. (2007) which suggests that for dynamical downscaling, there may be an optimal domain size under certain climate conditions. However, these results also show that there is a large spread between the ensemble members in all the systems. The spread between the members was largest in the area where the observed polar low developed. This emphasizes the relation between unpredictability and physical-dynamical instability. This is why a probabilistic approach is superior to a single deterministic method when forecasting polar lows and other fast developing systems.

Chapter 6

Conclusions and ideas for further work

The main findings in this study indicate that the predictability in a limited area forecast of a polar low is highly sensitive to resolution, domain size and physical descriptions in the model. By increasing the resolution from 12km to 4km, UM-EPS shows improvements in the results compared to LAMEPS. However, the improvements are crucially dependent on the domain size. A larger domain provides more information it the forecast. In addition, the model results are sensitive to the physical representation of the stable boundary layer. The forecast from the big domain has highest sensitivity.

The effect of the downscaling is largest for extreme weather in the late phase of the forecast, when the results from the big domain agree the most with the observations. This shows that the time of warning of a high impact weather event can be increased by employing a very high resolution, limited area ensemble prediction system. Nevertheless, it is evident that results from the small domain are more constrained by LAMEPS than those of the big domain. This indicates that when setting up a new limited area domain for downscaling, a careful consideration of the size and location of the domain is needed. It is not given that a smaller domain yields a better forecast even with higher resolution. A combination of the domain size and the information enhancements needs to be considered, along with the cost of running very high resolution models.

In this study, two new methods to verify the model results against observation data have been carried out. These two methods have great potential and need to be further explored. The pseudo satellite images show promising results, and compared to HIRLAM pseudo satellite images, the advantage of increasing the horizontal resolution is evident. In the near future it is planned to utilize the pseudo satellite images method for UM outputs in operational weather forecasting in the same manner as HIRLAM pseudo satellite images are used today. For the tracking algorithm, only a small part of the valuable information obtained was explored here. The spatial and temporal distributions of the genesis or lysis of the cyclones was not investigated, neither was the different strengths of the tracks. As described in section 3.2.2, the additional constraints introduced by Zahn and Storch (2008) did not reduce the number of detected tracks. If even further additional constraints along each individual track were introduced, the number of tracks could be reduced. New constraints may include requiring the feature points to have a strong vertical velocity within a search radius, or demanding a reversed

wind shear to be present. These two criteria are typically characteristic of polar lows, and in this manner the falsely identified vortices could be excluded.

The effect of the improved initial conditions has not been investigated in detail in this study. However, preliminary results (from different studies, not presented here) show that targeting observations can either improve the forecasts or damage the forecasts. In order to investigate whether the improved initial conditions have enhanced or worsened the results, ensemble systems should be run and analyzed. It is not sufficient to run a deterministic forecast, for one cannot know whether the results agreeing with observations are a result of skill or luck. It would be interesting to do this experiment with an initial time 24 hours later, i.e. 18 UTC 03.03.08. At this time the observed polar low was in the analysis.

To describe deep convection adequately with a NWP model, a horizontal resolution on the order of 1-2 km is necessary. Therefore further experiment may include performing this case study with UM run on 1 km horizontal grid mesh. Also, since UM is run with only 38 vertical levels compared to 60 in HIRLAM, it would be interesting to run UM with 70 vertical levels, which is the number of levels in the most recent version of UM. Also, for future work, it could be interesting to only downscale the members that span the most spread, instead of all the members. This will reduce the cost of running all the ensemble members. In addition, by combining the members from the experiments with the original setup and the perturbed run (lessvertical), a new ensemble system with 40+2 members will be obtained. In this way model uncertainty would be included.

These results indicate that the limited area forecasts are sensitive to domain size and physical descriptions. However, we have only performed the ensemble forecasts on one case. Several cases should be performed to achieve confidence in the results.

Appendix A

Parameterization schemes in UM

Boundary layer turbulence:

Boundary layer turbulence is parameterized with the scheme of Lock et al. (2000). The scheme describes the fluxes above the surface and it is parameterized over 13 model layers. The boundary layer can be stable, unstable or neutral depending on the direction of the heat-flux between the ground and the atmosphere. Its conditions are dependent on the diurnal cycle as well as the weather conditions. The turbulent fluxes can be calculated for momentum or the scalars of heat, and it is parameterized with the equation:

$$\overline{w'x'} = -K_x \frac{dx}{dz}, \tag{A.1}$$

where K_x is the vertical eddy diffusivity for x (i.e. heat, momentum), w is the vertical velocity and z is the height above the surface. K_x is parameterized with respect on the state of the boundary layer. The primes on w' and x' signifies eddy deviations due to turbulence, and the Reynolds averaging is denoted with an overbar.

The unstable boundary layer is characterized by strong vertical exchange and therefore the layer is well mixed and the eddy diffusivity parameter is then calculated from a shape function which spans the depth of the boundary later.

In the stable boundary layer, the vertical exchange is suppressed and this allows the layer to be more stratified and shallower than under unstable conditions. With the Prandtl number, P_t, the eddy diffusivity for the momentum (K_m) and heat (K_h) is related, i.e. $P_t = K_m/K_h$. In UM the set-up assumes $P_t = 1$, which yields $K_m = K_h$. The diffusivity for momentum and heat are then expressed as:

$$K_x = \lambda^2 Sf(Ri), \tag{A.2}$$

where S is the vertical wind shear, λ is a mixing length, and f is a stability function which decays with increasing Richardson number (Ri). Ri is a function describing the stability and the vertical wind shear in the atmosphere (Ri $= \frac{static-stability}{(wind-shear)^2}$). McCabe and Brown (2007) did a study where they investigated the effect of the surface heterogeneity on the vertical mixing in the stable boundary layer. They suggested that areas with

63

little orographic variability induce less vertical mixing in the SBL than areas with more complex topography. The vertical mixing in UM can be set by choosing between two stability functions, the long tail function and the sharp tail function. They are both dependent on Ri and describe the vertical mixing in the layer. The long tail function is given by:

$$f_{long-tails}(Ri) = \frac{1}{1 + 10Ri} \tag{A.3}$$

And the sharp function of King et al. (2001) is

$$f_{sharp}(Ri) = \begin{cases} (1 - 5Ri)^2 & 0 \leq Ri < 0.1, \\ \left(\frac{1}{20Ri}\right)^2 & Ri \geq 0.1. \end{cases} \tag{A.4}$$

Since the long tail function decays more slowly than the sharp tail function with increasing Ri, the long tail function yields more mixing in the stable boundary layer. Therefore UM in operational use at met.no is run with the long tail function which yields enhanced vertical mixing in SBL. This is due to the complex topography in Norway. The two domains used in this study are mainly over ocean, therefore the sharp tail function should better represent the stable boundary layer. For this reason we have performed an extra set of experiments, where the sharp function is chosen.

The convection scheme:

The convection scheme in UM represent the transport of heat, moisture and momentum associated with cumulus convection within a grid box and it is based on the convection scheme of Gregory and Rowntree (1990). The convection is parameterized with a CAPE (Convective Available Potential Energy) based buoyancy closure scheme, where convective momentum transport is included, and a radiative representation of anvil clouds. The scheme is modified by Roberts (2003) where the mass flux at the cloud base is limited. This is done on the basis where 4-km models tend to have a different behavior according to whether or not the convective parameterization is included (Lean et al., 2008). When there is no convection parameterized, the model organizes the precipitation in a good way, but tends to delay the convective initiation and then produce too few showers. This results in too heavy showers and too much precipitation is produced. Also, explicit convection may not produce precipitation when only small showers are expected. With the standard convection parameterization included, the showers are not always explicitly represented since the instability required is removed by the parameterization. This yields poor organization and underestimation of the showers. The scheme modified by Roberts (2003) allows the large showers in the model to be generated explicitly, but still the weaker convective clouds are represented. In the study of Lean et al. (2008) these different ways to represent the convection were investigated, and when compared with observation data, the modified convection scheme had, to some extent, a delay in the initiation of precipitation due to spin up effect, but aside from that it showed an apparent advantage.

The large scale cloud scheme and large scale precipitation scheme:

UM uses the cloud scheme of Smith (1990), which is based on a statistical parameterization method. The growth or decay of a cloud droplet radius changes instantaneously in water vapor or saturation, and the fluctuations about the grid-box mean vapor and liquid water content are parameterized with a symmetric triangular probability density function (PDF). In addition there is a prescribed critical value of relative humidity, RH_{crit}, which RH needs to exceed before clouds can form. The cloud scheme of Smith (1990) has also been modified to include ice cloud consistent with the Wilson and Ballard (1999) microphysics scheme (also called the large scale precipitation scheme). This involves a method which represents the mixed phase cloud cover microphysics, and in this way; vapor, cloud water, ice and rain are treated as prognostic variables, and describes the moisture in the atmosphere. The microphysical processes are treated as transfer terms between water vapor, cloud water, rain and ice and in this manner the large scale precipitation scheme describes the downward transfer of water in the atmosphere.

The radiation scheme:

The radiation scheme described by Ingram et al. (2004) includes short (SW) and long (LW) wave radiation. In the atmosphere SW and LW are to a high extent scattered, and it is very expensive to calculate all the directions of the radiation. By making approximations about the angular distribution of the radiation, the SW and LW are treated as downward and upward flux, respectively. The radiation scheme also includes cloud microphysics.

Sub surface, surface and layer processes:

Sub-surface, surface and layer processes are parameterized with the MOSES 2.2 scheme which describes the fluxes of heat, momentum, moisture and carbon at the surface and it is based on the scheme of Essery et al (2001). The scheme includes nine different surface types over 4 subsurface levels, and the surface energy balance is calculated at each grid point, respectively for each surface type. The surface temperature (T0m) is calculated from the surface energy balance.

Other processes:

In addition in UM there is a gravity wave scheme, which includes flow blocking and orographic drag. Aerosol modeling is not included in the setup used here.

Bibliography

Anderson, D., Hodges, K. I., and Hoskins, B. J. (2003). Sensitivity of Feature-Based Analysis Methods of Storm Tracks to the Form of Background Field Removal. *Monthly Weather Review*, 131:565–573.

Bader, M. J., Forbes, G. S., Grant, J. R., Lilley, R. B. E., and Waters, A. J. (1995). *Images in weather forecasting*. Cambridge University Press.

Blechschmidt, A. M. (2008). A 2-year climatology of polar low events over the Nordic Seas from satellite remote sensing. *Geophysical Research Letters*, 35.

Branković, C., Matjaćić, B., Ivatek-Šahdan, S., and Buizza, R. (2008). Downscaling of ECMWF Ensemble Forcasts for Cases of Severe Weather: Ensemble Statistics and Cluster Analysis. *Monthly Weather Review*, 136:3323–3342.

Bratseth, A. M. (1985). A note on CISK in polar air masses. *Tellus*, 37A:403–406.

Buizza, R. (2002). Chaos and weather prediction. *European Centre for Medium-Range Weather, internal report; Meteorological Training Course*, pages 1–28.

Buizza, R., Miller, M., and Palmer, T. N. (1999). Stochastic representation of model uncertainties in the ECMWF Ensemble Prediction System. *Q. J. R. Meteorological Society*, 125:2887–2908.

Buizza, R. and Palmer, T. N. (1995). The Singular-Vector Structure of the Atmospheric Global Circulation. *Journal of the Atmospheric Sciences*, 52:1434–1456.

Deng, A. and Stauffer, D. R. (2006). On improving 4-km mesoscale model simulations. *Journal of Applied Meteorology and Climatology*, 45:361–381.

Emanuel, K. A. and Rotunno, R. (1989). Polar lows as arctic hurricanes. *Tellus*, 41A:1–17.

Frogner, I.-L., Haakenstad, H., and Iversen, T. (2006). Limited-area ensemble predictions at the Norwegian Meteorological Institute. *Q. J. R. Meteorol. Soc.*, 132:2785–2808.

Frogner, I.-L. and Iversen, T. (2001). Targeted ensemble prediction for northern Europe and parts of the north Atlantic Ocean. *Tellus*, 53A:35–55.

Frogner, I.-L. and Iversen, T. (2002). High-resolution limited-area ensemble predictions based on low-resolution targeted singular vectors. *Q. J. R. Meteorol. Soc.*, 128:1321–1341.

Froude, L. S. R., Bengtsson, L., and Hodges, K. I. (2007a). The predictbility of Extratropical Storm Tracks and the Sensitivity of Their Prediction of the Observing System. *Monthly Weather Review*, 135:315–333.

Froude, L. S. R., Bengtsson, L., and Hodges, K. I. (2007b). The prediction of Extratropical Storm Tracks by the ECMWF and NCEP Ensemble Prediction Systems. *Monthly Weather Review*, 135:2545–2567.

Gregory, D. and Rowntree, P. R. (1990). A mass flux convection scheme with representation of cloud ensemble characteristics and stability-dependent closure. *Monthly Weather Review*, 118:1483–1506.

Gustafsson, N., Källen, E., and Thorsteinsson, S. (1998). Sensitivity of forecast errors to initial and lateral boundary conditions. *Tellus*, 50A:167–185.

Harold, J. M., Bigg, G. R., and Turner, J. (1999). Mesocyclone Acticity over the North-East Atlantic. Part 1: Vortex distribution and Variability. *International Journal of Climatology*, 19:1187–1204.

Hartmann, D. L. (1994). *Global Physical Climatology*. Academic Press.

Hodges, K. I. (1994). A General Method for Tracking Analysis and its Application to Meteorological Data. *Monthly Weather Review*, 120:2573–2586.

Hodges, K. I. (1995). Feature Tracking on the Unit Sphere. *Monthly Weather Review*, 123:3458–3465.

Hodges, K. I. (1999). Adaptive Constraints for Feature Tracking. *Monthly Weather Review*, 127:1362–1373.

Hohenegger, C. and Schär, C. (2007). Atmospheric predictability at synoptic versus cloud-resolving scales. *Bull. American Meteorological Cociety*, 88:1783–1793.

Hoskins, B. J. and Hodges, K. I. (2002). New perspective on the Northern Hemisphere Winter Storm Tracks. *Journal of the Atmospheric Sciences*, 59:1041–1061.

Hoskins, B. J. and Hodges, K. I. (2005). New perspective on the Southern Hemisphere Storm Tracks. *Journal of the Atmospheric Sciences*, 18:4108–4129.

Ingram, W., Woodward, S., and Edvards, J. (2004). Radiation. *Unified Model Documentation Paper 23*, version 4.0.

IPY (2009). IPY homepage: http://www.polararet.no/.

IPY-THORPEX (2009). IPY-THORPEX campaign homepage: http://www.ipy-thorpex.no/.

Jensen, M. H., Frogner, I.-L., Iversen, T., and Vignes, O. (2006). Limited area ensemble forcasting in Norway using targeted EPS. *ECMWF Newsletter No. 107.*

Kalnay, E. (2003). *Atmospheric Modeling, Data Assimilation and Predictability.* Cambridge University Press.

King, J. C., Connolley, W. M., and Derbyshire, S. H. (2001). Sensitivity of modelled Antarctic climate to surface and boundary-layer flux parametrizations. *Q. J. R. Meteorol. Soc.*, 127:689–719.

Kolstad, E. W. (2006). A new climatology of favourable conditions for reverse-shear polar lows. *Tellus*, 58A:344–354.

Laprise, R., Varma, M. R., Denis, B., Caya, D., and Zawadzki, I. (2000). Predictability of a Nested Limited-Area Model. *American Meteorological Society*, 128:4149–4154.

Lean, H. W., Clark, P. A., Dixon, M., Roberts, N. M., Fitch, A., Forbes, R., and Halliwell, C. (2008). Characteristics of High-Resolution Versions of the Met Office Unified Model for Forecasting Convection over the United Kingdom. *Monthly Weather Review*, 136:3408–3424.

Lock, A. P., Brown, A. R., Bush, M. R., Martin, G. M., and Smith, R. B. (2000). A new boundary layer mixing scheme. Part 1: Scheme description and single-column model tests. *Monthly Weather Review*, 128:3187–3199.

Lorenz, E. N. (1963). Deterministic Nonperiodic Flow. *Journal of the Atmospheric Sciences*, 20:130–141.

Lorenz, E. N. (1969). The predictability of a flow which possesses many scales of motion. *Tellus*, 21:289–307.

Mass, C. F., Ovens, D., Westrick, K., and Colle, B. A. (2002). Does increasing horizontal resolution produce more skullfull forecasts. *Bull. American Meteorological Society*, 83:407–430.

Molteni, F., Buizza, R., Palmer, T. N., and Petroliagis, T. (1996). The ECMWF Ensemble Prediction System; Methodology and validation. *Q. J. R. Meteorological Society*, 122:73–119.

Montgomery, M. T. and Farrell, B. F. (1992). Polar Low Dynamics. *Journal of the Atmospheric Sciences*, 49:2484–2505.

Noer, G. and Ovhed, M. (2003). Forecasting of Polar Lows in the Norwegian and the Barents Sea. *Proceedings of the 9th meeting of EGS Polar Lows Working Group, Cambridge, UK.* Available: http://www.uni-trier.de/index.php?id=28161#c60628.

Nordeng, T. E. and Rasmussen, E. A. (1992). A most beautiful polar low. A case study of a polar low development in the Bear Island region. *Tellus*, 44A:81–99.

Palmer, T., Buizza, R., Hagedorn, R., Lawrence, A., Leutbecher, M., and Smith, L. (2005/2006). Ensemble prediction: A pedalogical perspective. *ECMWF Newsletter. No. 106*, pages 10–17.

Rasmussen, E. A. (1979). The polar low as an extratropical CISK disturbance. *Q. J. R. Meteorological Society*, 105:531–549.

Rassmussen, E. A. and Turner, J. (2003). *Polar Lows. Mesoscale Weather Systems in the Polar Regions*. Cambridge University Press.

Roberts, N. M. (2003). The impact of a change to the use of the convection scheme to high-resolution simulations of convective events. *Met Office Technical Report*, 407:30pp.

Roberts, N. M. and Lean, H. W. (2007). Scale-Selective Verification of Rainfall from High-Resplution Forecasts of Convective Events. *Monthly Weather Review*, 136:78–97.

Smith, R. N. B. (1990). A scheme for predicting layer clouds and their water contents in a General Circulation Model. *Q. J. R. Meteorol. Soc.*, 116:435–460.

Staniforth, A., White, A., Wood, N., Thuburn, J., Zerroukat, M., and Cordero, E. (2002). Joy of U.M. 5.3 - Model Formulation. *Unified Model Documentation Paper No 15*.

Tijm, S. (2004). Hirlam pseudo satellite images. *Hirlam newsletter 46*, pages 59–64.

UK Met Office (2004). Unified Model User Guide.

van der Grijn, G. (2002). Tropical cyclone forecasting at ECMWF: new products and validation. *Technical Memorandum No. 386*.

Wilson, D. R. and Ballard, S. P. (1999). A microphysically based precipitation scheme for the UK Meteorological Office Unified Model. *Q. J. R. Meteorol. Soc.*, 125:1607–1636.

Xue, Y., Vasic, R., Janjic, Z., Mesinger, F., and Mitchell, K. E. (2007). Assessment of Dynamic Downscaling of the Continental U.S Regional Climate Using the Eta/SSiB Regional Climate Model. *Journal of Climate*, 20:4172–4193.

Yanase, W. and Niino, H. (2006). Dependence of Polar Low Development on Baroclinicity and Physical Processes: An Idealized High-Resolution Numerical Experiment. *Journal Of The Atmospheric Sciences*, 64:3044–3067.

Zahn, M. and Storch, H. V. (2008). Tracking Polar Lows in CLM. *Meteorologische Zeitschrift*, 17:445–453.